

A model of Ganymede's magnetic and plasma environment during the Juno PJ34 flyby

Aaron Stahl^{1,2}, Peter Addison¹, Sven Simon^{1,2}, Lucas Liuzzo³

¹School of Earth and Atmospheric Sciences, Georgia Institute of Technology, Atlanta, GA, USA

²School of Physics, Georgia Institute of Technology, Atlanta, GA, USA

³Space Sciences Laboratory, University of California, Berkeley, CA, USA

Key Points:

- Using a hybrid model, we provide three-dimensional context for plasma and magnetic field observations from the Juno PJ34 flyby of Ganymede
- Escaping heavy ions from Ganymede's ionosphere cause subtle, but discernible modifications to the magnetic field in the vicinity of the moon
- Ganymede's sub-Jovian magnetopause is susceptible to Kelvin-Helmholtz instabilities, causing the location of the boundary layer to oscillate

14 Abstract

15 Using a hybrid model (kinetic ions, fluid electrons), we provide context for plasma and
16 magnetic field observations from Juno's PJ34 flyby of Ganymede on 07 June 2021. We
17 consider five model configurations that successively increase the complexity of Ganymede's
18 atmosphere and ionosphere by including additional particle species and ionization mech-
19 anisms. We examine the density and flow patterns of pick-up ions with small (H_2^+), in-
20 termediate (H_2O^+), and large (O_2^+) masses in Ganymede's interaction region. The re-
21 sults are validated by comparing the modeled magnetic field and ion densities against
22 time series from Juno's magnetometer and plasma instruments. Our major findings are:
23 (a) Ganymede's internal dipole dominated the magnetic field signature observed inside
24 the moon's magnetosphere, while plasma currents shaped the field perturbations within
25 the "wake" region detected along the Jupiter-averted magnetopause. (b) Ganymede's
26 pick-up tail leaves a subtle, but clearly discernible imprint in the magnetic field down-
27 stream of the moon. (c) Heavy pick-up ions dominate ionospheric outflow and form a
28 tail with steep outer boundaries. (d) During the flyby, the position of Ganymede's Jupiter-
29 facing magnetopause varied in time due to Kelvin-Helmholtz waves traveling along the
30 boundary layer. As such, the location of the Jupiter-facing magnetopause observed by
31 Juno represents only a single snapshot of this time-dependent process. (e) Ionospheric
32 hydrogen ions are partially generated outside of Ganymede's magnetopause, forming a
33 dilute H_2^+ corona that surrounds the moon's magnetosphere. (f) Most H_2O^+ ions are
34 produced at low latitudes where field lines are closed, resulting in a very dilute pick-up
35 tail for this species.

36 **1 Introduction**

37 Jupiter's third Galilean moon, Ganymede, is the largest moon in the solar system
 38 with a radius of $R_G = 2,634.1$ km and orbits its parent planet at a distance of 15 Jupiter
 39 radii ($R_J = 71,492$ km). Ganymede's orbit is nearly circular and coincides with the planet's
 40 rotational equatorial plane. The moon is embedded within Jupiter's expansive magne-
 41 tosphere, whose magnetopause possesses a ramside stand-off distance of at least $45 R_J$
 42 (e.g., Joy et al., 2002; Connerney et al., 2017). Ganymede is the only satellite known to
 43 possess an intrinsic global magnetic field (Gurnett et al., 1996; Kivelson et al., 1996). This
 44 intrinsic field is largely dipolar (Kivelson et al., 2002; Weber et al., 2022) and driven by
 45 dynamo action in a metallic molten core (Anderson et al., 1996; Schubert et al., 1996).
 46 It generates an equatorial surface field magnitude of 719 nT, which is at least 6 times
 47 that of the ambient Jovian magnetospheric field (Kivelson et al., 2002). Jupiter's dipole
 48 moment is tilted at 9.6° relative to its spin axis, causing the Jovian magnetic equator
 49 to sweep over the moon twice each synodic rotation period (about 10 hours, see Kivelson
 50 et al. (2004) or Saur et al. (2010)). The time-varying horizontal magnetospheric field com-
 51 ponent experienced by Ganymede reaches magnitudes of up to about 80 nT. Its oscil-
 52 lations generate an induced field from the subsurface ocean located 150 km to 250 km
 53 beneath Ganymede's surface (Kivelson et al., 2002; Saur et al., 2015). The magnitude
 54 of this induced field is at most 6% that of the intrinsic field at the moon's surface (Kivelson
 55 et al., 2002).

56 Ganymede has a dilute atmosphere predominantly composed of O₂ at low altitudes
 57 and H₂ above a few hundred kilometers (e.g., Marconi, 2007; Leblanc et al., 2017). High-
 58 sensitivity spectral images acquired by the Hubble Space Telescope (HST) recently re-
 59 vealed H₂O in Ganymede's dayside atmosphere, suggesting it to be the dominant species
 60 around the subsolar point (Roth et al., 2021; Leblanc et al., 2023). Analysis of Lyman-
 61 α emissions observed by HST also recently confirmed the presence of an extended hy-
 62 drogen corona around the moon (Alday et al., 2017; Roth et al., 2023). Electron den-
 63 sity profiles derived from plasma wave observations and radio occultation measurements
 64 suggest that Ganymede is surrounded by an ionosphere, consisting largely of O₂⁺ and H₂⁺
 65 as well as minor contributions from O⁺ and H⁺ (e.g., Eviatar et al., 2000; Eviatar, Va-
 66 syliunas, & Gurnett, 2001; Carnielli et al., 2019; Buccino et al., 2022). The moon also
 67 exhibits auroral emissions driven by electron excitation of atmospheric molecules. These
 68 emissions are primarily observed along two oval-shaped regions enclosing Ganymede's

69 polar regions at high latitudes (Hall et al., 1998; Feldman et al., 2000; McGrath et al.,
 70 2013; Molyneux et al., 2018). Oscillations in the locations of the auroral ovals on the same
 71 time scale as Jupiter's synodic rotation were observed by HST. These oscillations were
 72 used to show the presence of an inductive response from the moon's subsurface ocean
 73 (Saur et al., 2015).

74 The ambient plasma environment at Ganymede is populated with charged parti-
 75 cles primarily originating from Io (Bagenal et al., 2016; Kim et al., 2020). These par-
 76 ticles are transported radially outward through flux tube interchange (Bagenal & De-
 77 lamere, 2011) and co-rotate at 80% of Jupiter's rotation velocity near Ganymede's or-
 78 bit (Williams, Mauk, & McEntire, 1997; Williams, Mauk, McEntire, Roelof, et al., 1997).
 79 The bulk velocity of the magnetospheric plasma exceeds the moon's Keplerian speed by
 80 about an order of magnitude. Therefore, the flow overtakes Ganymede with a relative
 81 velocity of 120–160 km/s (Kivelson et al., 2004). The upstream magnetospheric plasma
 82 is sub-Alfvénic and sub-magnetosonic (e.g., Kivelson et al., 2004; Jia & Kivelson, 2021),
 83 so no bow shock is formed upstream of Ganymede. The moon is tidally-locked with Jupiter,
 84 resulting in the same hemisphere always oriented toward the upstream flow. At Ganymede's
 85 orbit, the Jovian magnetospheric plasma is confined to an equatorial sheet with a num-
 86 ber density $n(d) = n_0 \exp \left[-\left(d/H \right)^2 \right]$, where d is the distance to the center of the sheet,
 87 $H \approx 3R_J$, and $n_0 \approx 10^7 \text{ m}^{-3}$ (Bagenal & Delamere, 2011). This plasma sheet lies be-
 88 tween Jupiter's magnetic and centrifugal equators, imparting a synodic periodicity to
 89 Ganymede's environment: the plasma density varies by up to a factor of 5 as the sheet
 90 passes over the moon (Jia & Kivelson, 2021).

91 Ganymede's strong intrinsic field carves out a mini-magnetosphere within Jupiter's
 92 magnetosphere, decelerating the incident plasma flow in the orbital trailing hemisphere
 93 and diverting it around the moon's internal field (e.g., Gurnett et al., 1996; Volwerk et
 94 al., 1999; Kivelson et al., 2004; Jia et al., 2008). As a result, field lines become draped
 95 over the moon and Alfvén wings are formed at larger distances to Ganymede (Neubauer,
 96 1980, 1998; Kivelson et al., 2002, 2004). These Alfvén wings connect to Jupiter's polar
 97 ionosphere, generating auroral footprints (Grodent et al., 2009; Bonfond et al., 2013, 2017;
 98 Hue et al., 2022). Ganymede's mini-magnetosphere can be divided into distinct regions
 99 of different field line geometries: “open” field lines emerge from the moon's high-latitude
 100 regions, connecting to Ganymede at one end and Jupiter at the other. The open field
 101 lines funnel energetic magnetospheric particles toward the moon's polar regions (e.g., Paty

& Wingdale, 2004; Fatemi et al., 2016; Jia & Kivelson, 2021). On the other hand, “closed” field lines emerge from low-latitude regions and connect to Ganymede at both ends (Jia & Kivelson, 2021). The boundary between these regions is referred to as the open-closed field line boundary (OCFB) and coincides with the locations of the moon’s auroral ovals (e.g., Saur et al., 2015; Duling et al., 2022). Magnetic field lines at mid-to-high latitudes in Ganymede’s tail region are open and allow particles to enter or escape the moon’s magnetosphere (Frank et al., 1997; Williams, Mauk, & McEntire, 1997; Williams, Mauk, McEntire, Roelof, et al., 1997). In the upstream hemisphere, closed field lines generated by Ganymede’s internal dipole extend about 30° north and south from the magnetic equator and up to $2 R_G$ from the surface (e.g., Williams, Mauk, & McEntire, 1997; Kivelson et al., 1998; Jia et al., 2008). The closed field lines in the downstream hemisphere span approximately half the latitude compared to the trailing hemisphere (e.g., Duling et al., 2014). Downstream, Ganymede’s mini-magnetosphere extends up to $\sim 10 R_G$ along the flow direction (e.g., Kivelson et al., 2004; Jia & Kivelson, 2021).

Ganymede’s internal dipole moment is tilted 176° from its spin axis and therefore its field is oriented nearly anti-parallel to the ambient Jovian field near the moon’s equator (Kivelson et al., 2002). This configuration results in favorable conditions for magnetic reconnection (Kaweeyanun et al., 2020; Jia & Kivelson, 2021). Reconnection occurs at Ganymede’s ramside magnetopause and in its magnetotail, and was identified as the primary mechanism for energy and plasma transfer from Jupiter’s magnetosphere into Ganymede’s local interaction region (Kaweeyanun et al., 2020). Observed surface brightness asymmetries between the (bright) leading and (dark) trailing hemispheres of Ganymede were suggested to be the result of reconnection in the magnetotail accelerating particles toward the moon’s surface (e.g., Khurana et al., 2007; Fatemi et al., 2016). High flow shear along Ganymede’s magnetopause flanks also supports the development of Kelvin-Helmholtz instabilities in these regions (Masters, 2017; Kaweeyanun et al., 2021).

Our knowledge of Ganymede’s magnetic and plasma environment is largely based upon in-situ measurements acquired by the Galileo spacecraft, which performed six close flybys of the moon between June 1996 and December 2000, as well as remote observations by the HST. The six Galileo flybys are denoted by their respective orbits and referred to as G1, G2, G7, G8, G28, and G29. The trajectories of these flybys are pictured in Figure 1, which uses the Ganymede-centered Cartesian GPhiO coordinate system. In this system the positive x -axis points in the corotational flow direction, the positive z -

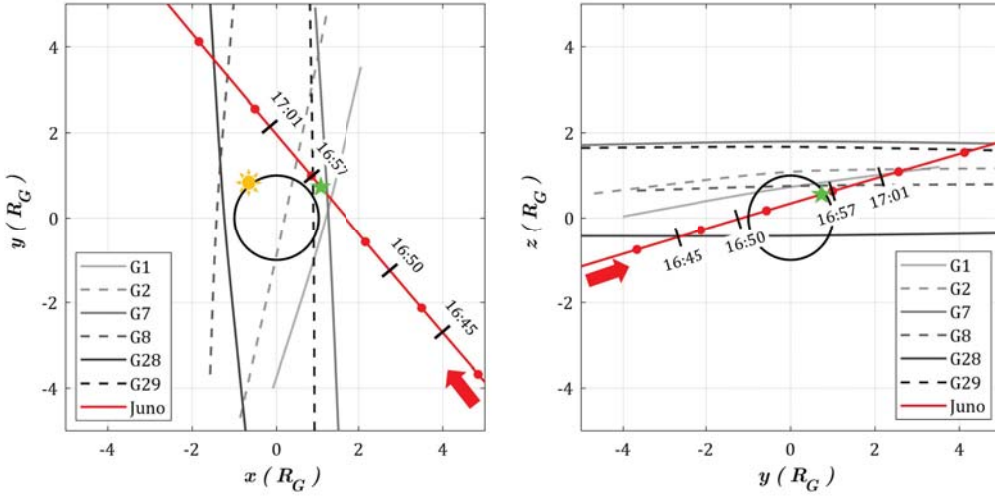


Figure 1. Trajectories of the six Galileo (gray lines) and one Juno (red line) close flybys of Ganymede in the (left) $z = 0$ and (right) $x = 0$ planes using the GPhiO Cartesian coordinate system (see text for definition). The small red circles along the Juno trajectory represent 5 minute time intervals starting at 16:42:00 UTC. The green star designates the point of Juno’s closest approach at an altitude of 1,046 km ($0.40 R_G$) at 16:56:08 UTC on 7 June 2021. The red arrows indicate the direction of motion of the Juno spacecraft, and Ganymede itself is represented by a circle of radius $1 R_G$. Transitions between regions of different plasma properties along the Juno trajectory (as described in Allegrini et al. (2022)) are identified by black bars and labeled with the corresponding times in UTC. Details on these features are discussed in the text. The observed “wake” region identified in Juno data by Allegrini et al. (2022) are entered at about 16:45 UTC and exited around 16:50 UTC. Juno’s inbound and outbound crossings of Ganymede’s magnetopause occurred at approximately 16:50 and 17:01 UTC, respectively. The marker at 16:57 UTC identifies the transition from nightside (before marker) to dayside (after marker) and the yellow sun in the $z = 0$ plane indicates the subsolar point during the Juno flyby.

axis points northward along the Jovian spin axis, and the y -axis completes the right-handed system with the positive pointing toward Jupiter. The distance from the origin of the GPhiO system is denoted by r . The components of the magnetic field \mathbf{B} in this system are referred to as (B_x, B_y, B_z) . Among the Galileo flybys G8 was the only one that occurred when Ganymede was located near the center of the Jovian magnetospheric plasma sheet (Jia & Kivelson, 2021). During this flyby, the Galileo spacecraft passed through Ganymede’s upstream magnetopause at low latitude where it detected a significant in-

crease to the B_z component generated by strong currents along the boundary layer, with B_z flipping sign from about -100 nT just outside the moon's magnetosphere to $+80$ nT within. Low frequency oscillations suggested to be Kelvin-Helmholtz surface waves were observed during the G8 flyby near both the inbound and outbound crossings of Ganymede's magnetopause (Kivelson et al., 1998).

The other five Galileo flybys occurred when the moon was well above (G1, G2, G29) or well below (G7, G28) the center of the Jovian plasma sheet. These encounters also saw sharp rotations of the magnetic field when entering and exiting Ganymede's magnetosphere. The G28 flyby passed through the upstream magnetopause at low latitude in the moon's southern hemisphere and detected field enhancements in B_z and B_x due to magnetopause currents and field line draping, respectively. However, the field line draping and compression of Ganymede's magnetosphere are both weak when the moon is located far from the center of the Jovian plasma sheet. As a result, the magnetic field observations from these five Galileo flybys can largely be explained by a superposition of Ganymede's internal dipole and the ambient Jovian field. Due to the strong plasma interaction at the time of G8, such an approach is not suitable for that flyby (e.g., Kivelson et al., 1998, 2004; Jia et al., 2008).

On 7 June 2021, about 14 hours before reaching its 34th perijove (PJ34), the Juno spacecraft performed the first and only targeted flyby of Ganymede since Galileo over 20 years prior. It reached a closest-approach altitude of 1,046 km ($0.40 R_G$) over the moon's leading hemisphere. The flyby occurred when the incoming solar radiation was directed along the unit vector $(0.67, -0.74, 0.00)$ in GPhiO coordinates, leaving the leading hemisphere mostly in shadow (Hansen et al., 2022) and the dawn terminator located 48° clockwise from the positive y axis in the $z = 0$ plane (see Figure 1 for reference). As shown in Figure 1, Juno approached the moon's downstream hemisphere from the Jupiter-averted half space and traveled toward upstream and Jupiter. The spacecraft moved from $-z$ to $+z$ during the encounter and passed the moon's leading hemisphere at low-to-mid latitude. Juno approached Ganymede on the nightside and transitioned to the dayside just after closest approach (see Figure 1), subsequently exiting the moon's mini-magnetosphere. Similar to G8, the Juno flyby occurred when Ganymede was located in the high density environment near the center of the Jovian plasma sheet (e.g., Valek et al., 2022; Weber et al., 2022), marking the first flyby in the downstream region under these conditions.

174 Juno's magnetometer (Connerney et al., 2017) detected significant field perturba-
 175 tions upon entry into Ganymede's interaction region (16:45 to 16:50 UTC in Figure 1),
 176 as B_z increased from about -65 nT to 0 nT at 16:45 UTC and the field magnitude reached
 177 a minimum of just below 10 nT at 16:46 UTC. A non-zero field component normal to
 178 the magnetopause was observed during the outbound magnetopause crossing (17:01 UTC),
 179 providing evidence for reconnection occurring at this location during the flyby (Romanelli
 180 et al., 2022). Juno's Waves Instrument (Kurth et al., 2017) measured the electron den-
 181 sity of Ganymede's magnetosphere, revealing distinct differences between the nightside
 182 and dayside hemispheres. The nightside electron density gradually increased from about
 183 $5 \cdot 10^6$ m $^{-3}$ to $15 \cdot 10^6$ m $^{-3}$ and then abruptly jumped to $30 \cdot 10^6$ m $^{-3}$ when transition-
 184 ing to the dayside at approximately 16:57 UTC (see Figure 1). The electron density then
 185 dropped to $5 \cdot 10^6$ m $^{-3}$ as Juno exited Ganymede's magnetosphere (Kurth et al., 2022).
 186 A radio occultation experiment conducted during the ingress detected signatures of Ganymede's
 187 ionosphere, finding a peak electron density of $(2 \pm 0.5) \cdot 10^9$ m $^{-3}$ near the surface (Buccino
 188 et al., 2022). This value is approximately half of the previously established upper limit
 189 from Galileo's radio occultation observations at Ganymede (Kliore, 1998).

190 Measurements from the Jovian Auroral Distributions Experiment (JADE, see Mc-
 191 Comas et al., 2017) characterized the cold (ionospheric) and thermal (ambient Jovian)
 192 electron and ion distributions during the flyby. JADE provided novel insights into the
 193 composition of the ion populations near Ganymede, since Galileo's Plasma Experiment
 194 could not infer the composition of outflowing ionospheric ions (e.g., Frank et al., 1997;
 195 Eviatar, Vasyliunas, & Gurnett, 2001). Inside the moon's magnetosphere, JADE detected
 196 mainly slow, cold ions alongside precipitating protons moving along the magnetic field
 197 lines. These observations indicate that Juno intersected a region of open field lines, al-
 198 lowing for the exchange of plasma between Ganymede's magnetosphere and its environ-
 199 ment (Allegrini et al., 2022). The population of cold ions in Ganymede's pick-up tail was
 200 observed to consist of O $^+$, O $_2^+$, H $^+$, H $_2^+$, and H $_3^+$ (Valek et al., 2022). Whereas the most
 201 abundant light ion species (H $_2^+$) was observed to be approximately symmetric in den-
 202 sity and energy about the inbound and outbound legs of Juno's flyby, the observed O $_2^+$
 203 ions achieved maximum density nearly 2 minutes after closest approach at 16:58 UTC
 204 (Valek et al., 2022). The "wake" region, indicated in Figure 1 from 16:45 to 16:50 UTC,
 205 was identified in Juno plasma observations (Allegrini et al., 2022) and is located down-
 206 stream and outside of the Jupiter-averted flank of Ganymede's magnetopause. JADE

207 detected ions with a mass-to-charge ratio of 3 within this region, which are assumed to
 208 be H_3^+ that either leaked out of Ganymede's magnetosphere or were created in the wake
 209 from H_2^+ reacting with atmospheric H_2 (Valek et al., 2022; Allegrini et al., 2022).

210 Various models have been applied to provide three-dimensional context for Galileo
 211 and Juno observations from the Ganymede flybys. The ion gyroradii in the ambient Jo-
 212 vian plasma near Ganymede are at most ~ 100 km (Kivelson et al., 2004). Therefore, this
 213 interaction scenario is in a regime where both fluid models and hybrid models (fluid elec-
 214 trons, kinetic ions) can accurately represent the plasma interaction. The first resistive
 215 MHD model of Ganymede's plasma interaction (Ip & Kopp, 2002) generated a prelim-
 216 inary description of the moon's magnetosphere and bolstered earlier postulations that
 217 field-aligned currents drive the observed ultraviolet auroral emissions (Feldman et al.,
 218 2000; Eviatar, Strobel, et al., 2001). Subsequently, a multi-fluid model was used to ex-
 219 plore Ganymede's magnetospheric structure and ionospheric outflow (Paty & Winglee,
 220 2004, 2006; Paty et al., 2008). It was found that the energy of ionospheric O^+ exiting
 221 Ganymede's magnetosphere along open field lines over the polar caps was largely below
 222 the detection threshold of Galileo's Plasma Experiment. The model thereby provided
 223 an explanation for the lack of O^+ outflow in observations from the polar G2 flyby (Frank
 224 et al., 1997; Paty et al., 2008). In combination with a brightness model of Ganymede's
 225 auroral emissions, Payan et al. (2015) applied a multi-fluid model to identify short-term
 226 (time scale of minutes) and long-term (time scale of hours) variability of the moon's au-
 227 roral brightness and morphology. These variabilities were suggested to correspond to re-
 228 connection processes at Ganymede's magnetopause and the moon's periodically chang-
 229 ing position relative to the center of the Jovian plasma sheet, respectively (Payan et al.,
 230 2015). Another multi-fluid model included higher-order velocity moments of Vlasov's equa-
 231 tion (namely, the pressure tensor and the heat flux tensor) in order to evaluate the role
 232 of electron physics in reconnection at Ganymede's magnetopause (Wang et al., 2018).
 233 It was shown that the anisotropies in electron pressure play an important role in shap-
 234 ing the electric field in the reconnection region.

235 The MHD model of Jia et al. (2008, 2009, 2010) added a model of the spatially non-
 236 uniform anomalous resistivity to Ganymede's interaction region (Jia et al., 2008, 2009,
 237 2010). In this model, reconnection is triggered only in regions where the local current
 238 density exceeds a certain threshold. The authors demonstrated that reconnection at Ganymede's
 239 upstream magnetopause occurs in intermittent bursts on time scales of 10s of seconds,

despite ambient conditions that vary on much larger time scales of several hours. The MHD model of Duling et al. (2014) incorporated realistic boundary conditions for the magnetospheric currents at the moon's insulating surface by requiring that the radial component of the electric current vanishes at the surface. This model quantified the impact of plasma interaction currents on the magnetic field near Ganymede's surface during the G8 flyby. It was found that the field magnitude in regions threaded by closed field lines is reduced by up to 120 nT compared to a mere superposition of Ganymede's internal field and Jupiter's magnetospheric field. In the polar regions, the field magnitude was comparably enhanced.

Dorelli et al. (2015) described Ganymede's magnetosphere within the framework of Hall MHD. Their model showed the appearance of large-scale flux transfer events in the moon's magnetopause and magnetotail, with the bulk flow directed away from Jupiter. These flows resulted in the formation of asymmetric Kelvin-Helmholtz waves along the magnetopause boundary, with the amplitudes being larger along the Jupiter-facing than the Jupiter-averted magnetopause. Additionally, the strongest field-aligned currents in the Hall MHD model occurred near the OCFB, suggesting that the Hall effect may contribute to the observed locations of Ganymede's auroral ovals (Dorelli et al., 2015). Tóth et al. (2016) coupled a Hall MHD model to a particle-in-cell model, providing kinetic treatment of electrons and ions in regions close to Ganymede. The model revealed flux transfer events along the moon's magnetopause that possessed magnetic signatures consistent with those observed during the Galileo flybys. These flux transfer events occurred in similar regions and on similar time scales as the previously identified signatures of bursty reconnection along the magnetopause (Jia et al., 2010). Zhou et al. (2019) utilized a similar combination of MHD and particle-in-cell models to calculate the flux densities of ions and electrons accelerated by reconnection at Ganymede's magnetopause. This study suggested that precipitation of energetic electrons, accelerated within the upstream reconnection region, contributes up to half of the peak brightness of Ganymede's auroral emissions (Zhou et al., 2019).

Several authors used hybrid simulations in conjunction with a particle tracing model to calculate maps of the precipitating energetic ion fluxes onto Ganymede's surface (Fatemi et al., 2016; Poppe et al., 2018), finding strong correlation between the modeled influx patterns and observed surface brightness asymmetries (Khurana et al., 2007). These results suggest that non-uniform influx of energetic magnetospheric ions is the primary driver

of the moon's surface brightness patterns (Fatemi et al., 2016). Based on a similar hybrid model, Fatemi et al. (2022) showed that the Hall effect dominates ion dynamics at Ganymede's magnetopause and that velocity distributions of ions in this region are highly anisotropic: the velocity component parallel to the background Jovian magnetospheric field was revealed to significantly exceed the perpendicular component. Liuzzo et al. (2020) used particle tracing in conjunction with field output from a hybrid model to study the spatial distribution of energetic electron flux onto Ganymede's surface. This study revealed that electrons contribute an order of magnitude more than ions to the charged particle number flux bombarding the moon's polar regions. These authors found their modeled electron influx patterns to be highly inhomogeneous, having locally reduced fluxes in the trailing hemisphere where the protection by the perturbed electromagnetic fields is strongest.

Recently, Duling et al. (2022) studied Ganymede's magnetosphere during Juno's PJ34 flyby using an MHD model. The poleward emission edges of the moon's auroral ovals, as observed by Juno during the PJ34 flyby (Greathouse et al., 2022), were found to deviate in latitude by less than 1° from the OCFB produced by this model on the downstream side. Thus, these results support the notion of the auroral emissions being generated near the OCFB (see also McGrath et al., 2013). The model results of Duling et al. (2022) also suggest that Juno's trajectory during the flyby did not intersect the region of closed field lines near Ganymede's wakeside surface. In order to evaluate the geometry of the closed field line region during the Juno flyby, Romanelli et al. (2022) modeled Ganymede's magnetosphere during the flyby using a hybrid approach. This hybrid model (Romanelli et al., 2022) suggests that the extension of the closed field line region toward downstream is larger than in the MHD results of Duling et al. (2022), and that the Juno spacecraft traversed this region for several minutes near closest approach.

None of the preceding modeling studies investigated the structure and dynamics of Ganymede's tail of ionospheric pick-up ions. Given the recent availability of Juno observations from Ganymede's mid-range tail region, there is strong motivation to understand how different ionospheric species populate this domain. In this study, we combine the AIKEF hybrid model (Müller et al., 2011) with Juno magnetic field and plasma observations from the Ganymede flyby (Valek et al., 2022; Allegrini et al., 2022) to provide three-dimensional context for these datasets. The AIKEF model includes a multi-species ionosphere around Ganymede and resolves the flow shear between different iono-

spheric and magnetospheric ion species. These features of the model may be necessary to explain plasma observations from the wake region and to search for Kelvin-Helmholtz instabilities along the magnetopause. We investigate how ionospheric models of increasing complexity populate the moon's tail region with pick-up ions and affect plasma and magnetic field signatures along Juno's trajectory. We also compare our results with data obtained from Juno's Jovian Auroral Distributions Experiment (JADE) and magnetometer (MAG) instruments. Additionally, we investigate the possible growth of Kelvin-Helmholtz instabilities in the vicinity of Juno's flyby trajectory as well as their influence on the observable plasma and magnetic signatures.

This paper is structured as follows: in section 2, we briefly introduce the AIKEF hybrid model and provide an overview of the input parameters for the various simulation setups. Our model results and their comparison against Juno observations are presented in section 3. Our investigation is concluded in section 4 with a brief summary of our major findings. In Appendix A, we provide additional evidence for the validity of our model by comparing its output against magnetometer observations from all six Galileo flybys of Ganymede.

2 Model Description

2.1 Hybrid Simulation Model AIKEF

To model Ganymede's near-space environment during the Juno PJ34 flyby, we apply the established hybrid code AIKEF (Müller et al., 2011). The AIKEF model treats electrons as a massless, charge-neutralizing fluid and ions as individual macroparticles. This kinetic treatment of the ions allows for the inclusion of physical processes arising from ion gyration, such as the Hall effect (e.g., Dorelli et al., 2015) and non-Maxwellian velocity distributions near the moon (e.g., Fatemi et al., 2022). In the wake region identified in plasma data just outside of Ganymede's Jupiter-avertered magnetopause (Allegrini et al. (2022) and Figure 1), Juno's magnetometer measured magnetic field magnitudes as low as ~ 10 nT over a region spanning 100s of km (e.g., Romanelli et al., 2022; Weber et al., 2022). In this environment, O_2^+ pick-up ions moving at speeds near the bulk velocity (120–160 km/s, see Kivelson et al., 2004) possess gyroradii of up to 4700 km ($1.8 R_G$). Thus, capturing the behavior of pick-up ions in this region requires a kinetic treatment of their dynamics.

The AIKEF model has been applied to other Galilean satellites of Jupiter, namely Callisto (Liuzzo et al., 2015, 2016, 2017, 2018, 2019a, 2019b, 2022) and Europa (Arnold et al., 2019; Arnold, Liuzzo, & Simon, 2020; Arnold, Simon, & Liuzzo, 2020; Breer et al., 2019; Addison et al., 2021, 2022, 2023). This hybrid code was also used extensively to model the plasma environment of Saturn's moon Titan (e.g., Simon et al., 2007; Tippens et al., 2022) and the interaction between the solar wind and Mercury's magnetic field (e.g., Müller et al., 2012). In the preceding studies of plasma interaction at Ganymede's neighbors Europa and Callisto, AIKEF achieved excellent quantitative agreement with Galileo observations of the magnetic field and plasma density (e.g., Müller et al., 2011; Liuzzo et al., 2016; Arnold et al., 2019). Notably, the model reproduced transitions between regimes dominated by field line draping and Callisto's induced dipole field (Liuzzo et al., 2016), as well as a localized magnetic perturbation consistent with a water vapor plume at Europa (Arnold et al., 2019). These examples demonstrate that the AIKEF model can generate quantitatively accurate representations of moon-magnetosphere interactions in the Jovian system. We provide additional model validation in Appendix A, where AIKEF output is compared against magnetometer observations from all six Galileo flybys of Ganymede.

Our study consists of five different model setups, successively increasing in the complexity of the applied atmosphere and ionosphere models. This approach enables us to identify which model components play a critical role in shaping the magnetic and plasma signatures observed by Juno during the PJ34 flyby. In this section, we first review the magnetospheric upstream parameters common to all five setups (see Table 1). Next, we discuss the atmosphere and ionization parameters specific to each setup (see Table 2). In setup I, we study Ganymede without taking into account any atmosphere or ionosphere in order to establish a “baseline” for the associated plasma and field perturbations. Only the moon's internal magnetic field (including both permanent and induced dipole terms) is included in this run. Setup II introduces a symmetric O₂ atmosphere exposed to uniform electron impact ionization. A symmetric H₂ atmosphere, again with a uniform electron impact ionization rate, is added for setup III. The objective of setups II and III is to study the outflow patterns of the dominant heavy (O₂⁺) and light (H₂⁺) ionospheric species, and to evaluate their impact on the magnetic field and plasma signatures near the moon. In setup IV, we add dayside photo-ionization for both atmospheric species (O₂ and H₂) in order to analyze the role of asymmetric ionosphere formation. Setup V

370 adds an H₂O atmospheric “bulge” concentrated around the dayside apex, with uniform
 371 electron impact and photo-ionization rates included. This setup accommodates the lat-
 372 est HST observations, which identified a persistent, localized H₂O bulge in Ganymede’s
 373 neutral envelope (Roth et al., 2021; Leblanc et al., 2023). This setup also facilitates the
 374 analysis of ionospheric flow dynamics for pick-up ions with intermediate weight (between
 375 O₂⁺ and H₂⁺).

376 Additional information on the AIKEF model can be found in Müller et al. (2011).
 377 Previous studies using AIKEF (e.g., Kriegel et al., 2011, 2014; Feyerabend et al., 2015)
 378 provide detailed coverage of the techniques for implementing atmospheres and ionospheres
 379 in the model, so only a brief description is provided here.

380 2.2 Hybrid Simulation Setup

381 Our hybrid model uses the Ganymede-centered GPhiO Cartesian coordinate sys-
 382 tem (described in Section 1), with a simulation domain spanning $-12 R_G \leq x \leq 18 R_G$,
 383 $-15 R_G \leq y \leq 15 R_G$, and $-20 R_G \leq z \leq 20 R_G$. Whenever an ion hits the surface
 384 of the moon or one of the six outer boundaries of the AIKEF model domain, it is deleted
 385 from the simulation. We utilize AIKEF’s hierarchical grid refinement structure to gen-
 386 erate three levels of resolution. The model setup consists of three nested cuboids, with
 387 Ganymede located near the center of the inner-most and highest resolution cuboid. When
 388 moving toward the moon, the grid cell size is reduced by a factor of two at each bound-
 389 ary between cuboids. From the innermost to outermost cuboid, the grid size and span
 390 of each refinement level are given by: $0.027 R_G$ for $-4 R_G \leq x \leq 6 R_G$, $|y|, |z| \leq 4 R_G$,
 391 then $0.054 R_G$ for $-6 R_G \leq x < -4 R_G$ and $6 R_G < x \leq 10 R_G$, $4 R_G < |y|, |z| \leq$
 392 $8 R_G$, and then $0.114 R_G$ for $-12 R_G \leq x < -6 R_G$ and $10 R_G < x \leq 18 R_G$,
 393 $|y|, |z| > 8 R_G$. Ionospheric ions drift toward downstream ($+x$) in the direction of the
 394 ambient Jovian plasma flow. Therefore, the region of increased grid resolution is extended
 395 farther in the downstream direction than toward upstream. The simulation is run un-
 396 til the upstream Jovian plasma has completed at least one full passage through the en-
 397 tire AIKEF domain, by which point the field configuration in the vicinity of Ganymede
 398 has reached a quasi-stationary state.

399 A summary of the model parameters characterizing the upstream flow is provided
 400 in Table 1. AIKEF treats the Jovian background field near Ganymede \mathbf{B}_0 as spatially

Table 1. Simulation parameters for the AIKEF model (common to all five setups)

Parameter	Symbol [unit]	Value	Source
Background magnetic field	\mathbf{B}_0 [nT]	(−15, 24, −75)	Duling et al. (2022)
Background field magnitude	B_0 [nT]	80.2	Duling et al. (2022)
Ganymede's magnetic moment (permanent)	\mathbf{M}_{dip} [$\times 10^{27}$ J/nT]	(−4.1, 9.0, −131.0)	Kivelson et al. (2002)
Ganymede's magnetic moment (induced)	\mathbf{M}_{ind} [$\times 10^{27}$ J/nT]	(1.2, −1.8, 0.0)	Kivelson et al. (2002)
Upstream plasma number density	n_0 [cm ^{−3}]	10	Jia and Kivelson (2021)
Upstream plasma mean ion mass	m_0 [amu]	14	Jia and Kivelson (2021)
Upstream plasma bulk velocity	\mathbf{u}_0 [km/s]	(130, 0, 0)	Jia and Kivelson (2021)
Upstream plasma ion temperature	$k_B T_0$ [eV]	100	Jia and Kivelson (2021)
Upstream plasma electron temperature	$k_B T_0$ [eV]	100	Jia and Kivelson (2021)
Convective electric field ($\mathbf{E}_0 = -\mathbf{u}_0 \times \mathbf{B}_0$)	\mathbf{E}_0 [mV/m]	(0, −9.8, −3.1)	(calculated)
Alfvén velocity ($V_{A,0} = \frac{B_0}{\sqrt{\mu_0 m_0 n_0}}$)	$V_{A,0}$ [km/s]	148	(calculated)
Alfvén Mach number ($M_{A,0} = \frac{u_0}{V_{A,0}}$)	$M_{A,0}$	0.88	(calculated)

uniform. As shown by Duling et al. (2022), this background field vector around closest approach to Ganymede is given by $\mathbf{B}_0 = (-15, 24, -75)$ nT. The moon's internal magnetic field is represented by the sum of the permanent dipole and induced magnetic moments, $\mathbf{M}_0 = \mathbf{M}_{\text{dip}} + \mathbf{M}_{\text{ind}}$ (see Table 1). Ganymede's permanent magnetic dipole moment is set to the value of $\mathbf{M}_{\text{dip}} = (-4.1, 9.0, -131.0) \times 10^{27}$ J/nT, as obtained by Kivelson et al. (2002) and analogous to Duling et al. (2022). Recently, Weber et al. (2022) performed an analysis across magnetometer data from three Galileo flybys and the Juno flyby to calculate updated spherical harmonic coefficients for Ganymede's intrinsic dipole moment. These authors arrived at a value of $\mathbf{M}_{\text{dip}} = (-4.9, 10.2, -130.9) \times 10^{27}$ J/nT, which is very close to our chosen value.

To represent the inductive response of Ganymede's subsurface ocean (e.g., Saur et al., 2015), we adopt the expression for the induced dipole moment given by Kivelson et al. (2002),

$$\mathbf{M}_{\text{ind}} = -\frac{2\pi\alpha R_{\text{G}}^3}{\mu_0} (B_{0,x}, B_{0,y}, 0) , \quad (1)$$

where $B_{0,x}$ and $B_{0,y}$ are the x and y components of the Jovian background field \mathbf{B}_0 . An “efficiency parameter” $\alpha = 0.84$ (Kivelson et al., 2002) is introduced to account for finite electrical conductivity of the ocean shell and a thickness well below $1 R_{\text{G}}$. As suggested by Kivelson et al. (2002), the phase lag of the induced field at Ganymede can be considered negligible. Thus, equation (1) yields $\mathbf{M}_{\text{ind}} = (1.2, -1.8, 0.0) \times 10^{27}$ J/nT for the conditions of the Juno encounter. While the maximum surface magnitude of the induced field is small (~ 15 nT) compared to the peak surface magnitude of the permanent dipole field (~ 1440 nT), it still meaningfully contributes to the x and y components of the moon's total magnetic moment \mathbf{M}_0 . In our model, Ganymede's total magnetic moment is then given by $\mathbf{M}_0 = (-2.9, 7.2, -131.0) \times 10^{27}$ J/nT.

At Ganymede's orbit, the impinging Jovian thermal plasma is composed of electrons, protons, and heavy ions like oxygen and sulfur (Kivelson et al., 2004; Bagenal et al., 2016; Kim et al., 2020). Consistent with preceding models (e.g., Jia et al., 2010; Fatemi et al., 2016, 2022; Duling et al., 2022; Romanelli et al., 2022), we use a singly charged ion species with mean mass $m_0 = 14$ amu to represent the thermal ion population incident upon the moon. The ambient Jovian ion and electron temperatures in our model are set to $k_B T_0 = 100$ eV (Kivelson et al., 2004; Jia & Kivelson, 2021). The average number density n_0 of the ambient Jovian magnetospheric plasma at Ganymede's orbit

433 varies from about 1 cm^{-3} to 10 cm^{-3} as a function of the moon's distance to the cen-
 434 ter of the Jovian plasma sheet, with the maximum value occurring at the center of the sheet
 435 (Bagenal & Delamere, 2011). Ganymede was located near the center of the Jovian
 436 plasma sheet during the Juno flyby (Hansen et al., 2022). We therefore use a number
 437 density of $n_0 = 10 \text{ cm}^{-3}$ for the incident plasma, which is in agreement with ion den-
 438 sity measurements obtained by Juno's JADE instrument a few minutes prior to enter-
 439 ing Ganymede's magnetosphere (Allegrini et al., 2022). Our choice of upstream density
 440 is also consistent with the electron densities of $5 - 12 \text{ cm}^{-3}$ measured by the Juno Waves
 441 instrument during PJ34, just outside of the moon's magnetosphere (Kurth et al., 2022).

442 Only the thermal component of the Jovian magnetospheric plasma is included in
 443 our model. Accounting for the energetic ion population (e.g., Clark et al., 2022) would
 444 require lowering the time step in AIKEF to below what is computationally feasible (e.g.,
 445 Liuzzo et al., 2019a, 2019b). The energetic ions only account for a small portion of the
 446 current density (Mauk et al., 2004; Kim et al., 2020), and therefore they do not make
 447 a significant contribution to the plasma interaction. As shown by several preceding hy-
 448 brid modeling studies, the inclusion of the energetic ions is *not* required to accurately
 449 reproduce spacecraft observations or global magnetospheric structures at Ganymede (e.g.,
 450 Fatemi et al., 2016, 2022; Poppe et al., 2018; Romanelli et al., 2022).

451 Upstream of Ganymede, the Jovian thermal plasma travels with a bulk velocity \mathbf{u}_0
 452 in the $(+x)$ direction. We choose a value of $|\mathbf{u}_0| = 130 \text{ km/s}$, which is within the range
 453 of sub-corotation velocities ($120 - 160 \text{ km/s}$) observed at Ganymede's orbit (e.g., Williams,
 454 Mauk, & McEntire, 1997; Krupp et al., 2004; Kivelson et al., 2004; Jia & Kivelson, 2021).
 455 Our choice of bulk velocity and upstream plasma density yields an Alfvénic Mach num-
 456 ber of $M_{A,0} = 0.88$ (see Table 1), which is consistent with the literature (e.g., Jia &
 457 Kivelson, 2021) and close to the values used in prior models (e.g., Jia et al., 2008; Fatemi
 458 et al., 2022; Duling et al., 2022). Outside of Ganymede's magnetosphere, the chosen pa-
 459 rameters yield a convective electric field $\mathbf{E}_0 = -\mathbf{u}_0 \times \mathbf{B}_0$ that points into the $y < 0$
 460 half space and also has a weak southward component (see Table 1).

461 2.3 Atmosphere and Ionosphere Models

462 Table 2 provides an overview of the atmosphere and ionosphere parameters used
 463 in each of the five AIKEF model setups (denoted I, II, III, IV, and V). Each setup builds

Table 2. Parameters of Ganymede's Atmosphere and Ionosphere in AIKEF

Parameter	Symbol [Unit]	(I)	(II)	Model Setup (III)	(IV)	(V)	Source
O ₂ column density	N_{O_2} [cm ⁻²]	-	1.5×10^{15}	1.5×10^{15}	1.5×10^{15}	1.5×10^{15}	Carnielli et al. (2020)
O ₂ scale height	H_{O_2} [km]	-	250	250	250	250	Hall et al. (1998)
O ₂ surface number density	$n_{O_2,0}$ [cm ⁻³]	-	6.0×10^7	6.0×10^7	6.0×10^7	6.0×10^7	(calculated)
O ₂ e-impact ionization rate	ν_{e^-, O_2} [s ⁻¹]	-	1.0×10^{-7}	1.0×10^{-7}	1.0×10^{-7}	1.0×10^{-7}	Carberry Mogan et al. (2023)
O ₂ photo-ionization rate*	ν_{p,O_2} [s ⁻¹]	-	-	-	3.0×10^{-8}	3.0×10^{-8}	Carberry Mogan et al. (2023)
H ₂ column density	N_{H_2} [cm ⁻²]	-	-	7.5×10^{14}	7.5×10^{14}	7.5×10^{14}	Marconi (2007)
H ₂ scale height	H_{H_2} [km]	-	-	1000	1000	1000	Shematovich (2016)
H ₂ surface number density	$n_{H_2,0}$ [cm ⁻³]	-	-	7.5×10^6	7.5×10^6	7.5×10^6	(calculated)
H ₂ e-impact ionization rate	ν_{e^-, H_2} [s ⁻¹]	-	-	6.0×10^{-8}	6.0×10^{-8}	6.0×10^{-8}	Carberry Mogan et al. (2023)
H ₂ photo-ionization rate*	ν_{p,H_2} [s ⁻¹]	-	-	-	3.1×10^{-9}	3.1×10^{-9}	Carberry Mogan et al. (2023)
H ₂ O column density**	N_{H_2O} [cm ⁻²]	-	-	-	-	4.8×10^{15}	Leblanc et al. (2023)
H ₂ O scale height	H_{H_2O} [km]	-	-	-	-	200	Vorburger et al. (2022)
H ₂ O surface number density**	$n_{H_2O,0}$ [cm ⁻³]	-	-	-	-	2.2×10^8	(calculated)
H ₂ O e-impact ionization rate	ν_{e^-, H_2O} [s ⁻¹]	-	-	-	-	1.0×10^{-7}	Carberry Mogan et al. (2023)
H ₂ O photo-ionization rate*	ν_{p,H_2O} [s ⁻¹]	-	-	-	-	2.1×10^{-8}	Carberry Mogan et al. (2023)

* Sunlit hemisphere only

** Value at subsolar point (see Figure 1)

upon the previous one by adopting its parameters and including additional atmospheric species and/or ionization mechanisms. Setup I represents a “baseline” run and does not include any atmosphere or ionosphere at all. This baseline setup functions as a reference for Ganymede’s plasma interaction region and will enable us to identify perturbations generated by the ionospheric species included in subsequent configurations. This setup is also similar to those employed by previous hybrid models (e.g., Fatemi et al., 2016, 2022; Poppe et al., 2018).

In setups II-IV, the neutral density of each species in Ganymede’s atmosphere is described by a barometric law,

$$n_s(r) = n_{s,0} \exp\left(-\frac{h}{H_s}\right) , \quad (2)$$

where $n_s(r)$ is the number density of neutral species s at altitude h above the moon’s surface, $n_{s,0}$ is the number density at the surface, and H_s is the corresponding scale height. The number density $n_{s,0}$ of neutral species s at Ganymede’s surface is related to the scale height H_s and column density N_s by $n_{s,0} = N_s/H_s$.

In setup II, we introduce O₂ as the only atmospheric species because several studies suggest it to be the most abundant molecule in Ganymede’s atmosphere (e.g., Marconi, 2007; Plainaki et al., 2015; Leblanc et al., 2017; Carnielli et al., 2020). Studies of Ganymede’s neutral O₂ envelope found an approximately radially symmetric distribution about the moon’s surface (e.g., Leblanc et al., 2017), which is consistent with the spherical symmetry inherent in our model atmosphere (see equation (2)). The O₂ scale height in our model is set to $H_{O_2} = 250$ km, which is inside the range of 100-1000 km proposed by Hall et al. (1998) and consistent with values used in previous modeling studies of Ganymede’s plasma interaction (e.g., Duling et al., 2014, 2022). The O₂ atmosphere is contained within the AIKEF model’s highest resolution cuboid (see Section 2.2), where the grid resolution accommodates 3.5 cells per scale height H_{O_2} . We assume an O₂ column density of $N_{O_2} = 1.5 \times 10^{15} \text{ cm}^{-2}$. This value is slightly above the upper limit of $1.0 \times 10^{15} \text{ cm}^{-2}$ placed by Hall et al. (1998) and slightly below the recent estimate of $2.5 \times 10^{15} \text{ cm}^{-2}$ by Carnielli et al. (2020). Leblanc et al. (2023) recently proposed an O₂ column density of about $4.0 \times 10^{14} \text{ cm}^{-2}$, which is also within a factor of 4 to the value we assume. Our chosen column density yields a surface O₂ number density of $n_{O_2,0} = 6.0 \times 10^7 \text{ cm}^{-3}$. Ionization of Ganymede’s neutral O₂ envelope is driven primarily by electron impact ionization, the rate of which is about 5 times greater than that of photo-

496 ionization (Carnielli et al., 2019; Carberry Mogan et al., 2023). In setup II, we include
 497 *only* electron impact ionization and adopt a constant (i.e., spatially uniform) ionization
 498 rate of $\nu_{e,O_2} = 1.0 \times 10^{-7} \text{ s}^{-1}$, in agreement with Carberry Mogan et al. (2023).

499 In setup III, we include an additional atmospheric species, H₂, which is suggested
 500 by numerous studies to be the second most abundant constituent of Ganymede's atmo-
 501 sphere and dominates at altitudes above 200 km (e.g., Marconi, 2007; Turc et al., 2014;
 502 Jia & Kivelson, 2021; Leblanc et al., 2023). Since the peer-reviewed literature does not
 503 provide any estimates of the scale height of H₂ at Ganymede, we set the value to $H_{H_2} =$
 504 1000 km, which is about half the estimated scale height of *atomic* hydrogen (e.g., Turc
 505 et al., 2014; Shematovich, 2016). The column density of H₂ is set to one half the column
 506 density of O₂, yielding $N_{H_2} = 7.5 \times 10^{14} \text{ cm}^{-2}$. This choice of N_{H_2} is consistent with
 507 models of the moon's atmosphere (e.g., Marconi, 2007; Shematovich, 2016; Leblanc et
 508 al., 2017), which found $N_{O_2}/N_{H_2} \approx 2\text{-}3$ over most of Ganymede's surface. Our H₂ col-
 509 umn density also agrees with the value of $6.1 \times 10^{14} \text{ cm}^{-2}$ recently proposed by Leblanc
 510 et al. (2023), who used new HST observations to constrain the densities of Ganymede's
 511 atmospheric species. Our choice of scale height and column density yield an H₂ surface
 512 number density of $n_{H_2,0} = 7.5 \times 10^6 \text{ cm}^{-3}$, nearly an order of magnitude lower than
 513 that of O₂. As with molecular oxygen, electron impact ionization is the primary ioniza-
 514 tion mechanism for H₂ at Ganymede and exceeds the photo-ionization rate by about a
 515 factor of 3 (Carberry Mogan et al., 2023). For setup III, we assume a uniform electron
 516 impact ionization rate of $\nu_{e,H_2} = 7.0 \times 10^{-8} \text{ s}^{-1}$, again adapted from Carberry Mogan
 517 et al. (2023). Analogous to setup II, this third model configuration does not take into
 518 account any contribution to Ganymede's ionosphere from photo-ionization.

519 In model setup IV, photo-ionization of O₂ and H₂ is added to the sunlit hemisphere
 520 of Ganymede (see Figure 1 and Table 2). The moon's atmosphere has a maximum op-
 521 tical depth of 0.03 (Carnielli et al., 2019), so the incoming solar radiation is not signif-
 522 icantly attenuated even close to the surface. Therefore, uniform photo-ionization rates
 523 of $\nu_{p,O_2} = 3.0 \times 10^{-8} \text{ s}^{-1}$ and $\nu_{p,H_2} = 3.1 \times 10^{-9} \text{ s}^{-1}$ for O₂ and H₂, respectively, are
 524 included in our model (Carnielli et al., 2019; Carberry Mogan et al., 2023).

525 For setup V, the model is again augmented by including a third atmospheric species:
 526 an H₂O density bulge is added about the subsolar point, as recently detailed by Roth
 527 et al. (2021) and Leblanc et al. (2023). To account for the concentration of H₂O around

528 Ganymede's dayside apex, we use a modified barometric law adopted from Cervantes and
 529 Saur (2022) and apply it to the moon's sunlit hemisphere only:

$$530 \quad n_{\text{H}_2\text{O}}(h, \vartheta) = \begin{cases} n_{\text{H}_2\text{O},0} \cos^\gamma(\vartheta) \exp\left(-\frac{h}{H_{\text{H}_2\text{O}}}\right) & \text{for } 0^\circ \leq \vartheta \leq 90^\circ \\ 0 & \text{for } 90^\circ < \vartheta \leq 180^\circ \end{cases}. \quad (3)$$

531 In this expression, ϑ represents the angle between the unit vectors pointing (1) from Ganymede's
 532 center to its subsolar point and (2) from the moon's center to a given point in its atmo-
 533 sphere. While Cervantes and Saur (2022) did not study Ganymede's atmosphere, these
 534 authors found that $\gamma = 6$ best represents the H_2O bulge observed by HST around Eu-
 535 ropa's subsolar point (Roth, 2021). Due to the similarity between the extent of the H_2O
 536 density bulges observed at Europa and Ganymede (Leblanc et al., 2023), we adopt $\gamma =$
 537 6 from Cervantes and Saur (2022) for our Ganymede model. Leblanc et al. (2023) found
 538 peak H_2O column densities of about $6 \times 10^{15} \text{ cm}^{-2}$ near the subsolar point when Ganymede's
 539 trailing hemisphere was illuminated, and about $1 \times 10^{15} \text{ cm}^{-2}$ when the moon's lead-
 540 ing hemisphere was illuminated. During the Juno flyby of Ganymede, nearly 75% of the
 541 trailing hemisphere was exposed to solar radiation (see Figure 1). Accordingly, we lin-
 542 early interpolate the maximum H_2O column density between these two cases to obtain
 543 a column density at the subsolar point of $N_{\text{H}_2\text{O}} = 4.8 \times 10^{15} \text{ cm}^{-2}$ in our model. Near
 544 Ganymede's terminator plane (i.e., $\vartheta \approx 90^\circ$), Roth et al. (2021) and Leblanc et al. (2023)
 545 found H_2O column densities below $1.0 \times 10^{13} \text{ cm}^{-2}$. This value is negligible compared
 546 to the column densities of O_2 and H_2 at the terminator. Therefore, we set $n_{\text{H}_2\text{O}}$ to zero
 547 in the terminator plane and in Ganymede's nightside hemisphere (see equation (3)).

548 In this study, we assume a scale height of $H_{\text{H}_2\text{O}} = 200 \text{ km}$, which is slightly larger
 549 than the value of 50 km proposed by Vorburger et al. (2022). However, our choice of $H_{\text{H}_2\text{O}}$
 550 allows the AIKEF simulation grid to fully resolve the radial structure of the H_2O enve-
 551 lope, while the region populated by H_2O still maintains a small size relative to Ganymede
 552 and the scale of the moon's plasma interaction region. The implications of our choice
 553 of $H_{\text{H}_2\text{O}}$ on the results will be addressed in Section 3.3. The maximum surface number
 554 density of H_2O at the dayside apex is then given by $n_{\text{H}_2\text{O},0} = 2.4 \times 10^8 \text{ cm}^{-3}$, which
 555 is about a factor of 4 and 30 greater than the (uniform) surface densities of O_2 and H_2 ,
 556 respectively. We expose H_2O to a uniform electron impact ionization rate of $\nu_{e,\text{H}_2\text{O}} =$
 557 $1.0 \times 10^{-7} \text{ s}^{-1}$ and a dayside photo-ionization rate of $\nu_{p,\text{H}_2\text{O}} = 2.1 \times 10^{-8} \text{ s}^{-1}$, again
 558 adapted from Carberry Mogan et al. (2023). Other neutral species (OH , O , and H) also
 559 inhabit Ganymede's atmosphere, but they possess negligible column densities compared

560 to those of O₂, H₂, and H₂O (e.g., Marconi, 2007; Leblanc et al., 2017). Therefore, these
 561 additional species are not included in our model. The inclusion of H₂O in setup V en-
 562 sures that the dynamics of ionospheric species across the entire range of ion gyroradii
 563 occurring at Ganymede are included in our model: from small (H₂⁺), to intermediate (H₂O⁺,
 564 but also representative of other water group species), to large (O₂⁺).

565 3 Model Results for Ganymede's Plasma Environment

566 3.1 Setup I: No Atmosphere or Ionosphere

567 In this section, we present the results from model setup I. The initial conditions
 568 for this setup include the Jovian magnetospheric background field and Ganymede's per-
 569 manent and induced dipole moments, but no atmosphere or ionosphere around the moon.
 570 Figure 2 displays two-dimensional illustrations of the modeled magnetic field components
 571 (B_x , B_y , B_z), magnetic field magnitude $|\mathbf{B}|$, Jovian plasma number density n_J , and bulk
 572 velocity magnitude $|\mathbf{u}_J|$ for this setup. All quantities in panels (a)-(f) are shown in the
 573 $y = 0$ plane of the GPhiO system, containing the center of Ganymede, the upstream
 574 flow velocity \mathbf{u}_0 , and the north-south component of the background field \mathbf{B}_0 . Panels (g)-
 575 (i) display the magnetic field components in the $x = 0$ plane, which is perpendicular
 576 to the upstream flow velocity. Magnetic field lines are plotted in black and Ganymede
 577 is indicated by a white circle about the origin of each panel.

578 The modeled open and closed field line regions of Ganymede's magnetosphere are
 579 visible in the $y = 0$ plane (Figures 2(a)-(d)) and the $x = 0$ plane (Figures 2(g)-(i)).
 580 Field lines connected to Ganymede on both sides comprise the closed field line region,
 581 while field lines that connect to the moon on one side, but exit the AIKEF model do-
 582 main on the other (i.e., connect to Jupiter), are “open”. Field lines that do not connect
 583 to Ganymede at all correspond to the background magnetospheric field outside of the
 584 moon's magnetosphere. In both the $y = 0$ and $x = 0$ planes (Figures 2(a)-(d) and 2(g)-
 585 (i), respectively), the open field lines emanate at high latitude from the moon's polar caps
 586 and the closed field lines are confined to near-equatorial latitudes. As shown in Figures
 587 2(a)-(d), our modeled closed field line region in the $y = 0$ plane extends upstream to
 588 about $x = -1.9 R_G$. The upstream extension of our modeled closed field line region
 589 is consistent with the results of Duling et al. (2022) and Romanelli et al. (2022), who both
 590 found this region to extend to about $x = -2.0 R_G$ during the Juno encounter (see Fig-

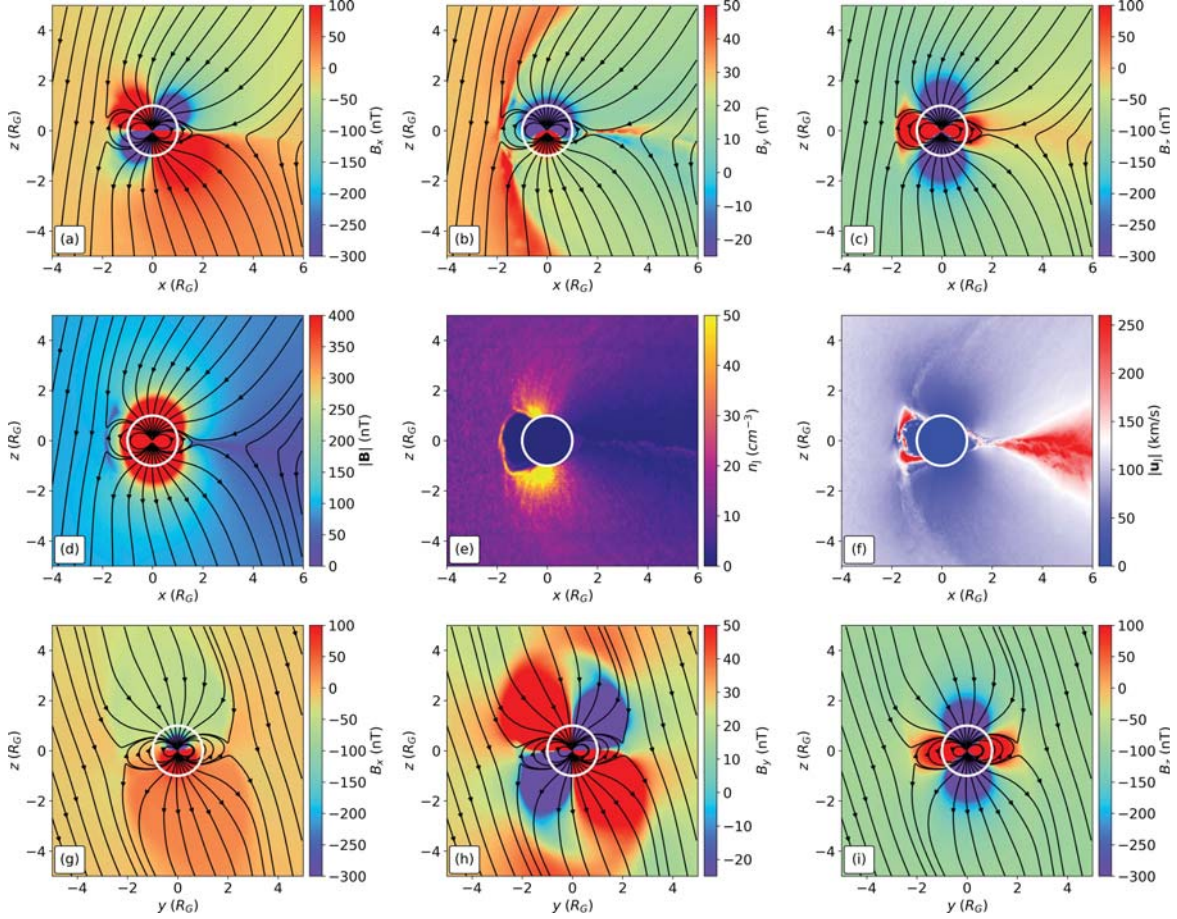


Figure 2. Two-dimensional color plots of AIKEF hybrid model results for setup I (no atmosphere or ionosphere; see Section 2.3 for details). For the $y = 0$ plane of the GPhiO coordinate system, the first two rows show: (a) B_x , (b) B_y , (c) B_z , (d) $|\mathbf{B}|$, (e) the number density of the Jovian magnetospheric plasma n_J , and (f) the bulk velocity magnitude of the Jovian plasma $|\mathbf{u}_J|$. Results for the $x = 0$ plane are displayed in the third row: (g) B_x , (h) B_y , and (i) B_z . In subplots (a)-(d) and (g)-(i), we also include a selection of magnetic field lines in black. Ganymede is denoted by the white circle of radius $1 R_G$ centered at the origin of each panel. To highlight the position of Ganymede's magnetopause, the B_y component in panels (b) and (h) utilizes different color scale limits than B_x and B_z .

ure 1 in either study). The modeled closed field line region in Figures 2(a)-(d) extends downstream to $x = +1.6 R_G$, which is approximately the same value as obtained by Duling et al. (2022). In contrast to this, Romanelli et al. (2022) suggest that the closed field line region reached farther downstream during the Juno flyby than in our model, extending slightly beyond $x = 2 R_G$.

Analogous to Saur et al. (2015), we determined the latitude of the OCFB on Ganymede's surface by tracing the magnetic field lines emanating from the surface at various latitudes of a given longitude, classifying each line as either open or closed. We find the OCFB to be located at surface latitudes of 48° N and 43° S in the upstream hemisphere of the $y = 0$ plane, and 22° N and 25° S in the downstream hemisphere (see Figures 2(a)-(d)). Our modeled OCFB latitudes are within a few degrees of the locations seen in the MHD simulations of Duling et al. (2022), and also coincide with the latitudes where the intensity of oxygen aurora emissions peaked during the Juno flyby (Greathouse et al., 2022).

Alfvén wings form above Ganymede's northern and southern polar caps, encompassing the open field lines that exit the moon's surface at high latitudes (Figures 2(a)-(d) and 2(g)-(i)). As shown by Neubauer (1980), the northern (−) and southern (+) Alfvén wing characteristics are oriented along $\mathbf{u}_0 \pm \frac{\mathbf{B}_0}{\sqrt{\mu_0 n_0 m_0}}$. The wings are therefore tilted toward downstream, with the B_x component reduced in the northern wing (green in Figures 2(a) and 2(g)) and increased in the southern wing (red in Figures 2(a) and 2(g)). Using Equation (1) from Simon et al. (2022) and the parameters from Table 1, we find that the Alfvén wings are tilted toward downstream with respect to \mathbf{B}_0 by 36.3° in the northern hemisphere and 46.2° in the southern hemisphere (see Figures 2(a)-(d)). This slight difference between the tilts of the two wings is produced by the component of the background field antiparallel to the corotation direction, $B_{0,x} = -15$ nT. In the $x = 0$ plane, the Alfvén wing characteristics form an angle of 11.3° with the z axis, pointing away from Jupiter (−) in the north and toward Jupiter (+) in the south (see Figures 2(g)-(i)).

The strong perturbations displayed near Ganymede in the B_x , B_y , and B_z components (Figures 2(a)-(d) and 2(g)-(i)) mainly stem from the superposition of the moon's internal dipole field with the Jovian magnetospheric background field. Ganymede's dipole field lines emanate outward from the southern polar cap ($z < 0$), turn northward and continue along loops of (approximately) constant latitude around the moon, and then return to Ganymede from above the northern polar cap ($z > 0$). As a result, the z component of the internal dipole field points southward (parallel to $B_{0,z}$) at high latitudes and northward (antiparallel to $B_{0,z}$) at low latitudes. Within the $x = 0$ and $y = 0$ planes, the superposition of Ganymede's internal dipole field and the primarily southward Jovian background field therefore produces two petal-shaped regions in B_z , where the moon's dipole amplifies the negative $B_{0,z}$ component of the background field (dark purple, see

Figures 2(c) and 2(i)). Near the equatorial plane, the positive perturbation imposed by the dipole weakens $|B_{0,z}|$. In the vicinity of Ganymede's surface, the B_z component even flips sign to become positive (red, see again Figures 2(c) and 2(i)). Since Ganymede's magnetic moment points approximately southward, the B_z signatures generated near the moon by the superposition of the internal dipole and the background field are nearly rotationally symmetric about the z axis. In three dimensions, B_z is therefore reduced within two bulb-shaped regions above the moon's polar caps (purple in Figures 2(c) and 2(i)), whereas the region of elevated B_z forms a torus along the moon's equator (red in Figures 2(c) and 2(i)).

In the $y = 0$ plane, Ganymede's internal dipole produces a shamrock-like pattern in the B_x component (purple and red in Figure 2(a)). As the moon's dipole field lines exit the southern polar cap, they bend toward upstream for $x < 0$ and toward downstream for $x > 0$. Superimposed with the (weak) negative $B_{0,x}$ component of the background field, this generates a region of negative B_x (purple) in the $(x < 0, z < 0)$ sector and a region of positive B_x (red) in the $(x > 0, z < 0)$ sector of the $y = 0$ plane (see Figure 2(a)). As the dipole field lines return to Ganymede in the northern hemisphere, they bend toward downstream for $x < 0$ and toward upstream for $x > 0$. This produces the regions of positive B_x (red) in the $(x < 0, z > 0)$ sector and negative B_x (purple) in the $(x > 0, z > 0)$ sector. The Alfvén wings, which show decreased B_x in the northern wing and increased B_x in the southern wing, slightly amplify the perturbations associated with the two "shamrock leaves" in the downstream hemisphere (Figure 2(a)).

The B_y component exhibits a similar, shamrock-like perturbation pattern in the $x = 0$ plane near the moon where the internal field is strong (red and purple in Figure 2(h)). Ganymede's dipole field curves away from the z axis for $z < 0$, corresponding to its bending toward Jupiter for $y > 0$ and away from Jupiter for $y < 0$. In the $(y < 0, z < 0)$ sector, this imposes a negative perturbation on the positive $B_{0,y}$ component of the background field, flipping the sign to negative (purple). Conversely, $B_{0,y}$ is amplified (red) by Ganymede's internal field in the $(y > 0, z < 0)$ sector (see Figure 2(h)). The reverse occurs in the northern hemisphere ($z > 0$) of the $x = 0$ plane, yielding positively (red, $y < 0$) and negatively (purple, $y > 0$) perturbed "shamrock leaves" in B_y .

661 The magnitude of the magnetic field $|\mathbf{B}|$, displayed in Figure 2(d), is enhanced by
 662 at least a factor of five in an envelope around Ganymede, resulting from the dominance
 663 of the moon's intrinsic dipole in this region (red in Figure 2(d)). The field magnitude
 664 $|\mathbf{B}|$ becomes depleted in a broad region downstream of $x \approx 3 R_G$, decreasing to nearly
 665 an order of magnitude below the Jovian magnetospheric background field $|\mathbf{B}_0|$ (dark blue
 666 in Figure 2(d)). This results from the impinging Jovian field lines being diverted around
 667 Ganymede's mini-magnetosphere.

668 The location of Ganymede's upstream magnetopause is best visible in the B_y com-
 669 ponent: Figure 2(b) reveals a sharp boundary between the upstream region of slightly
 670 enhanced B_y (orange-red) and the downstream region of slightly depleted B_y (blue-green).
 671 In our model, the magnetopause possesses a stand-off distance from the ramside surface
 672 of approximately $0.9 R_G$ (measured along the negative x axis). Observations from the
 673 Juno flyby do not directly constrain the ramside stand-off distance of Ganymede's mag-
 674 netopause, since the trajectory was mainly located in the downstream hemisphere (see
 675 Figure 1). However, the Galileo G8 flyby occurred under ambient conditions similar to
 676 those of the Juno flyby: Ganymede was positioned near the center of the Jovian mag-
 677 netospheric plasma sheet and the upstream density was comparable to the value used
 678 in our model (e.g., Kivelson et al., 2004; Allegri et al., 2022). During G8, Galileo crossed
 679 the upstream magnetopause at distances of $0.80 R_G$ (inbound) and $0.96 R_G$ (outbound)
 680 to Ganymede's surface. Both magnetopause crossings occurred at low latitudes and within
 681 15° longitude of the upstream apex (Kivelson et al., 1998). The locations of the mag-
 682 netopause crossings observed during G8 are in close agreement with our modeled ram-
 683 side stand-off distance for the Juno flyby. On the Jupiter-facing and Jupiter-averted flanks,
 684 Ganymede's magnetopause coincides with the outer boundary of the open field line re-
 685 gion (Figures 2(g)-(i)). The magnetopause also confines the $\pm y$ extent of the shamrock-
 686 like perturbation pattern in B_y (Figure 2(h)), as well as the perturbations to B_x gen-
 687 erated by draped Jovian field lines (Figure 2(g)).

688 Figure 2(e) displays the incident plasma being partially diverted around the up-
 689 stream magnetopause and funneled toward Ganymede's surface just poleward of the closed
 690 field lines, populating two cusp-like regions (bright yellow in Figure 2(e)). These cusps
 691 correspond to densities of up to 5 times the upstream value. Our modeled density pat-
 692 tern demonstrates that most thermal ions impinging onto Ganymede's magnetosphere
 693 do not have sufficient energy to access the moon's surface at low latitudes, where it is

“protected” by closed field lines (see also Cooper et al., 2001). Only a very small portion of the impinging ion population is able to penetrate the upstream magnetopause at low latitudes, with the number density dropping to below 1% of the upstream density above the moon’s ramside apex (dark purple in Figure 2(e)). The inflow pattern of the Jovian thermal ions seen in Figure 2(e) is consistent with the findings of prior models (e.g., Poppe et al., 2018; Fatemi et al., 2022). The high-density cusps correspond to regions of low plasma velocity above Ganymede’s poles (dark blue in Figure 2(f)): the velocity of the ions parallel (north) or antiparallel (south) to \mathbf{B} decreases when they travel along the “converging” field lines of the internal dipole. Downstream of Ganymede, the Jovian plasma density n_J is also depleted by a factor of about 10 (again depicted in dark purple). This reduction is generated by the diversion of the impinging flow around the moon’s magnetosphere. The regions of high plasma velocity near the upstream magnetopause and in the downstream tail region (Figure 2(f), red) are associated with local acceleration of the flow due to reconnection between antiparallel field lines from Jupiter and Ganymede (see also, e.g., Jia et al., 2009; Kaweeyanun et al., 2020; Romanelli et al., 2022).

Figure 3 displays time series of the magnetic field components B_x , B_y , and B_z , as well as the field magnitude $|\mathbf{B}|$, along Juno’s trajectory during the PJ34 Ganymede flyby. Juno magnetometer observations are represented by the solid black lines. Results from the AIKEF hybrid model are plotted as red lines. The “vacuum superposition model,” which is the superposition of the undisturbed Jovian magnetospheric background field and Ganymede’s internal dipole field, is plotted with blue lines. The vertical dashed lines indicate transitions between different sectors of Ganymede’s interaction region, as identified in plasma observations from the JADE instrument (Allegrini et al., 2022). The observed magnetic field displays strong perturbations along the flyby trajectory in all three components, mainly from Ganymede’s internal dipole, but also including contributions from plasma interaction currents. The deviation between the AIKEF model (red) and the vacuum superposition model (blue) at a given time indicates the modeled sign and magnitude of the contribution due to plasma currents.

We begin the discussion of Figure 3 by explaining the magnetic field signatures from the vacuum superposition model, which allows us to establish a “baseline” for the subsequent analysis of the time series from the AIKEF model and Juno. Ganymede’s internal dipole dominates the magnetic signature observed along the segment of Juno’s tra-

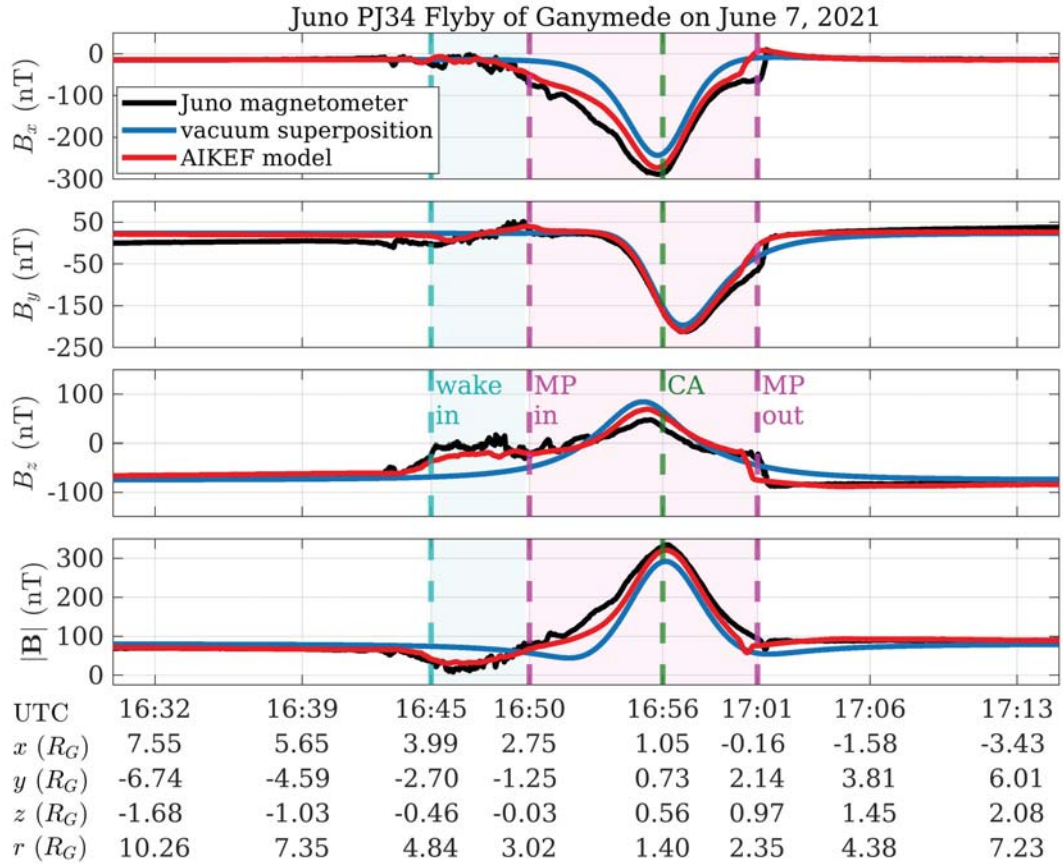


Figure 3. Observations and model results of the magnetic field components along Juno’s PJ34 flyby trajectory of Ganymede. Included from top-to-bottom are B_x , B_y , B_z (given in GPhiO coordinates), and the field magnitude $|\mathbf{B}|$. Each panel displays the Juno magnetometer observations (black lines), hybrid model output (red lines), and the vacuum superposition model (blue lines), i.e., a mere superposition of the Jovian magnetospheric background field and Ganymede’s internal dipole field. The dashed teal line denotes Juno’s entry into the “wake” region (Allegrini et al., 2022) at 16:45:08 UTC, while the dashed magenta lines denote the inbound (“MP in”) and outbound (“MP out”) magnetopause crossings at 16:49:48 and 17:00:39 UTC, respectively. These plasma regimes were identified by Allegrini et al. (2022) in data from the JADE instrument. The dashed green line (labeled “CA”) indicates Juno’s closest approach to Ganymede at 16:56:08 UTC and corresponding to an altitude of 1046 km ($0.40 R_G$). The light teal shading highlights the portion of Juno’s trajectory located within the wake region, whereas the light magenta shading spans the segment of the trajectory inside Ganymede’s magnetosphere. The location of Juno is provided below each timestamp along the bottom panel in GPhiO coordinates, with $r = \sqrt{x^2 + y^2 + z^2}$ denoting distance to the center of Ganymede.

jectory within the moon's magnetosphere (16:50 UTC to 17:01 UTC, shaded magenta in Figure 3). The magnitude of Ganymede's dipole field scales as a function of r^{-3} , where r is the distance to Ganymede's center. Therefore, the vacuum superposition model (blue lines in Figure 3) displays maximum perturbations near closest approach at 16:56 UTC. Except for in the immediate vicinity of Ganymede's magnetopause, the trajectory inside the moon's magnetosphere was confined to the ($x > 0, z > 0$) sector and Juno remained at northern latitudes below 30° N (Hansen et al., 2022). Near the moon, the dipole field lines sampled by Juno thus pointed northward and were bent toward the z axis. Around closest approach, Juno also resided in the sub-Jovian hemisphere ($y > 0$), where Ganymede's dipole field lines bend away from Jupiter.

Therefore, the vacuum superposition model displays negative perturbations to both B_x and B_y near Ganymede, reaching minimums of -243 nT and -197 nT, respectively, within about 20 seconds of closest approach. Along the inbound segment of the trajectory within the Jupiter-averted ($y < 0$) hemisphere, Juno was too far downstream and too close to the $z = 0$ plane (see Figure 1) to sample a region of the dipole field with positive B_y . In B_z , the vacuum superposition model displays a positive perturbation near the moon: Ganymede's dipole field imposes a perturbation on the background field component $B_{0,z} < 0$, initially reducing $|B_z|$ and then flipping the sign of B_z to a maximum of about 85 nT just prior to closest approach (blue line in the third row of Figure 3). This corresponds to Juno traveling through the torus-shaped region of increased B_z (red) in Figures 2(c) and 2(i).

Around Juno's entry into Ganymede's magnetosphere, the magnetic field magnitude of the vacuum superposition model dips below the Jovian magnetospheric background value. This corresponds to Juno's position between $x = 2 R_G$ and $x = 3 R_G$ downstream of Ganymede and close to the $z = 0$ plane, where the moon's dipole field points northward and depletes the predominantly southward background field \mathbf{B}_0 . As Juno approached Ganymede ($x \leq 2 R_G$), the perturbations in B_x and B_y (which increase the magnitudes of both components) map into the field magnitude of the vacuum superposition model and begin to dominate the behavior of $|\mathbf{B}|$. This causes the vacuum superposition model to display an enhancement in $|\mathbf{B}|$, reaching a maximum value of 292 nT near closest approach that is almost a factor of 4 above the background field strength $|\mathbf{B}_0| = 80$ nT.

We now discuss how the “vacuum” picture is affected by plasma interaction currents and how these currents generate the magnetic field signatures displayed by the AIKEF model and Juno observations. The “wake” region identified by Allegrini et al. (2022) resides just outside Ganymede’s magnetosphere, downstream of the moon and along the Jupiter-averted magnetopause flank. We note that this region is distinct from Ganymede’s “geometric” plasma wake, which is located directly downstream of Ganymede and defined by $x \geq 0$ and $\sqrt{y^2 + z^2} \leq R_G$. Juno observations within the wake indicate the presence of particles from both Ganymede’s ionosphere and the Jovian plasma sheet (Allegrini et al., 2022, and Section 1).

As shown in Figure 3, Juno crossed through the wake region slightly south of the equator from about 16:45 UTC to 16:50 UTC. During this time, the observed B_x component decreases gradually from the background value $B_{0,x} = -15$ nT to about $B_x = -55$ nT (top panel in Figure 3). The B_x component of the vacuum superposition model remains nearly constant over the same time, indicating that the observed decrease in B_x is produced by plasma interaction currents. As shown in Figure 3, the AIKEF model generates a similar reduction of B_x throughout the wake region. Neither the modeled (red line) nor the observed B_x component (black line) contain a distinct jump corresponding to the inbound magnetopause crossing, but rather B_x progressively decreases until closest approach. Within Ganymede’s magnetosphere, the dip in B_x from the internal dipole is amplified by field line draping in the northern Alfvén wing (which also reduces B_x ; green region in Figure 2(g)). In the time series from AIKEF, a minimum B_x value of -273 nT is reached near closest approach, which is slightly above the observed minimum of -288 nT. Within the moon’s magnetosphere, our model setup I persistently underestimates the strength of the observed dip in the B_x component, deviating by as much as 40 nT from the values seen by Juno (near 16:53 UTC, red versus black lines in the top panel of Figure 3). As we will show later, the inclusion of ionospheric pick-up ions in setups II-V results in the generation of stronger plasma currents near Ganymede, largely eliminating this deviation in B_x .

As indicated in Figure 3, Juno exited Ganymede’s mini-magnetosphere around 17:01 UTC and very close to the $x = 0$ plane. The magnetic field components in this plane are also depicted in Figures 2(g)-(i). During the outbound magnetopause crossing, Juno observed a sharp increase in B_x of about 60 nT over a distance of $0.2 R_G$. This jump is associated with the spacecraft exiting the region of reduced B_x inside the northern Alfvén

wing (green in Figure 2(g)). The AIKEF model displays a comparable jump in B_x at the outbound magnetopause crossing, both in magnitude and distance spanned. However, the modeled transition occurs about $0.2 R_G$ farther downstream and 1 minute earlier than observed, which is similar to the model results of Duling et al. (2022). For setup I, a deviation between modeled and observed magnetopause locations is indeed expected: due to the absence of Ganymede's ionosphere in the model, the counter pressure built up against the impinging Jovian flow is lower than in reality.

Similar to B_x , the observed B_y component in the wake region is not significantly affected by Ganymede's dipole (second panel in Figure 3). Instead, Juno observed a modest increase from the undisturbed (inbound) background field value of 5 nT to about 50 nT as a result of plasma interaction currents, shortly before exiting the wake at around 16:49 UTC. In the inbound segment of the trajectory, there is an offset of 19 nT between the background field in AIKEF ($B_{0,y} = 24$ nT, taken from Table 1) and the background B_y value of 5 nT observed by Juno. This stems from AIKEF using the average magnetospheric field at closest approach to determine \mathbf{B}_0 throughout the *entire* simulation domain. Whereas the B_y increase observed by Juno in the wake is about 45 nT, the enhancement displayed by AIKEF is a factor of 1.7 lower (about 26 nT). Inside Ganymede's magnetosphere, the moon's internal dipole dominates the B_y component. The B_y time series from the vacuum superposition model (blue), AIKEF model (red), and Juno observations (black) all largely overlap throughout the mini-magnetosphere until shortly before the outbound magnetopause crossing, indicating minimal perturbation to B_y from plasma currents inside of this region. During the outbound magnetopause crossing, the observed B_y component exhibits a similar jump as B_x , increasing by about 50 nT over a comparable distance of $0.2 R_G$ along the trajectory. Our model setup I does not reproduce the observed steepness of this transition and, similar to B_x , it again occurs about $0.2 R_G$ farther downstream than was measured by Juno.

The observed B_z component increases from the (inbound) background value of -60 nT at 16:43 UTC to about 0 nT at 16:45 UTC, immediately before Juno entered the wake region identified by Allegrini et al. (2022). The AIKEF model reproduces the steep inbound slope in B_z beginning near 16:43 UTC, but deviates from the observed B_z value at the inbound wake crossing (16:45 UTC) by about 20 nT. The observed positive B_z perturbation and slight deviation between AIKEF and the Juno data persist throughout the wake. The magnetic perturbations observed within the wake region will be re-

825 visited in Sections 3.2-3.3 when we include Ganymede's ionosphere: this region was found
 826 to be populated by pick-up ions (Allegrini et al., 2022) which may modify the plasma
 827 currents. However, we emphasize that even *without* the inclusion of Ganymede's iono-
 828 sphere, the modeled B_z component does reveal perturbations in the wake region, and
 829 the B_z perturbations calculated by AIKEF are similar to those observed by Juno. Thus,
 830 the inclusion of Ganymede's ionosphere is not required to make the wake region "vis-
 831 ible" in the magnetic field.

832 The observed contribution to B_z from plasma interaction currents flips sign (be-
 833 coming negative) inbound of closest approach, indicated by the observed B_z time series
 834 (black) dropping below the vacuum superposition model (blue) in Figure 3. As a result,
 835 the maximum B_z value of 47 nT observed by Juno remains nearly 40 nT below the max-
 836 imum value in the vacuum superposition model. In a similar way, AIKEF suggests the
 837 B_z signature from Ganymede's dipole to be weakened by the plasma interaction around
 838 closest approach. However, the effect is less pronounced than suggested by observations.
 839 Similar to the B_x and B_y components, the AIKEF model matches the sharpness and mag-
 840 nitude of the observed outbound magnetopause crossing in B_z , but the modeled mag-
 841 netopause is again displaced about $0.2 R_G$ toward downstream.

842 The field magnitude $|\mathbf{B}|$ observed by Juno decreases in the wake region to its min-
 843 imum value of around 10 nT. While in the wake, Juno traveled through the region down-
 844 stream of Ganymede's magnetosphere where our model displays depleted $|\mathbf{B}|$, and which
 845 is also intersected by the $y = 0$ plane (dark blue in Figure 2(d)). The plasma interac-
 846 tion in the wake reduces $|B_z|$ (see third panel of Figure 3), which maps into the field mag-
 847 nitude in this region. As can be seen from the bottom panel of Figure 3, our model setup
 848 I quantitatively reproduces the reduction of $|\mathbf{B}|$ within the wake. This again supports
 849 the notion that an ionosphere around Ganymede is not required to generate discernible
 850 field perturbations within this region. Around closest approach, both the observed $|\mathbf{B}|$
 851 and the field magnitude from AIKEF are dominated by Ganymede's internal dipole (blue
 852 versus black and red lines in the bottom panel of Figure 3). A maximum value of $|\mathbf{B}| =$
 853 334 nT is reached in Juno data just after closest approach, exceeding the peak value from
 854 the vacuum superposition model by about 40 nT. For both the AIKEF model and Juno
 855 observations, this overshoot of $|\mathbf{B}|$ above the vacuum superposition model is caused by
 856 the enhancement to $|B_x|$ from field line draping in the northern hemisphere (see Figures
 857 2(a) and 2(d)).

858 3.2 Setup II: Radially Symmetric O₂ Atmosphere Around Ganymede

859 In this section, we present the model results for setup II. This configuration uti-
 860 lizes the same parameters for the upstream plasma and Ganymede's internal field as model
 861 setup I, but now includes a symmetric O₂ atmosphere exposed to a uniform electron im-
 862 pact ionization rate (see Section 2.3). Figure 4 displays two-dimensional color plots of
 863 the number densities (panels (a)-(c)) and bulk velocities (panels (d)-(f)) for both ion species
 864 involved in the interaction. The projection of Juno's trajectory onto the cutting planes
 865 is indicated by the dashed green line. In Figure 5, we display the time series along the
 866 trajectory for the modeled ion number densities (Jovian and ionospheric) and the ob-

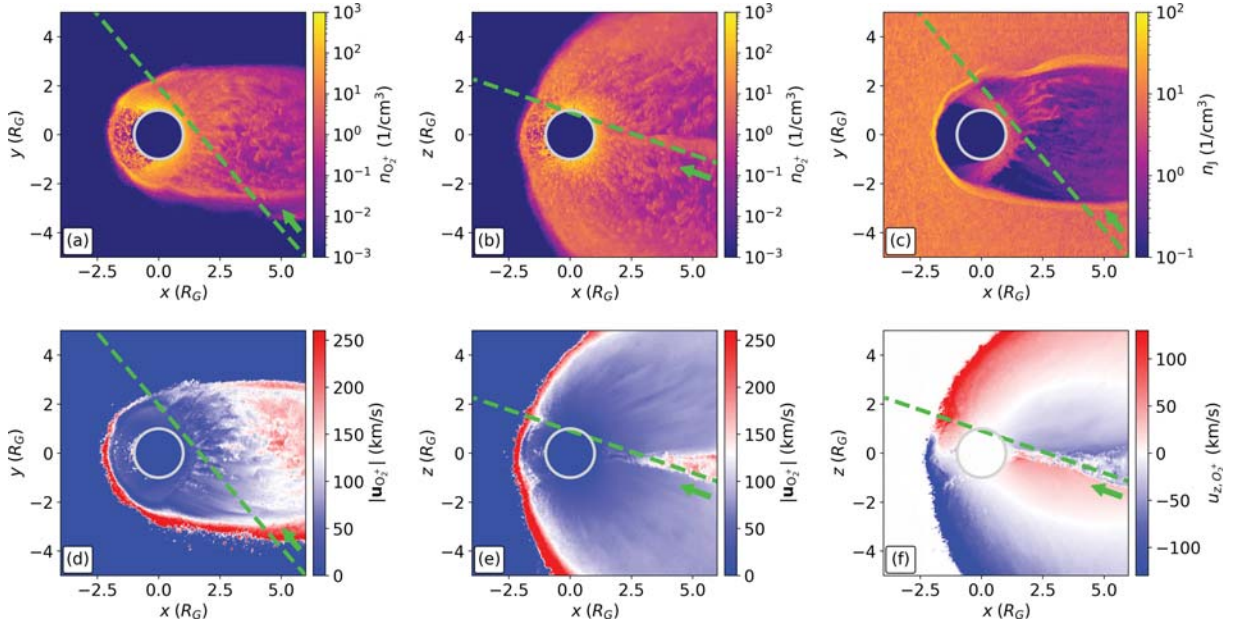


Figure 4. Two-dimensional color plots of the modeled Jovian plasma and ionospheric O₂⁺ flow for setup II, which includes a symmetric O₂ atmosphere with uniform electron impact ionization (see Section 2.3). The figure includes: (a) ionospheric O₂⁺ number density $n_{O_2^+}$ in the $z = 0$ plane, (b) $n_{O_2^+}$ in the $y = 0$ plane, (c) Jovian plasma number density n_J in the $z = 0$ plane, (d) ionospheric O₂⁺ velocity magnitude $|u_{O_2^+}|$ in the $z = 0$ plane, (e) $|u_{O_2^+}|$ in the $y = 0$ plane, and (f) the z component of the ionospheric O₂⁺ velocity u_{z,O_2^+} , again in the $z = 0$ plane. Regions with $u_{z,O_2^+} > 0$ are depicted in red, and regions where $u_{z,O_2^+} < 0$ are shown in blue. The projection of the Juno PJ34 flyby trajectory onto each plane is indicated by the dashed green line, with the arrow denoting the spacecraft's direction of travel. Ganymede corresponds to the light gray circle of radius 1 R_G centered at the origin.

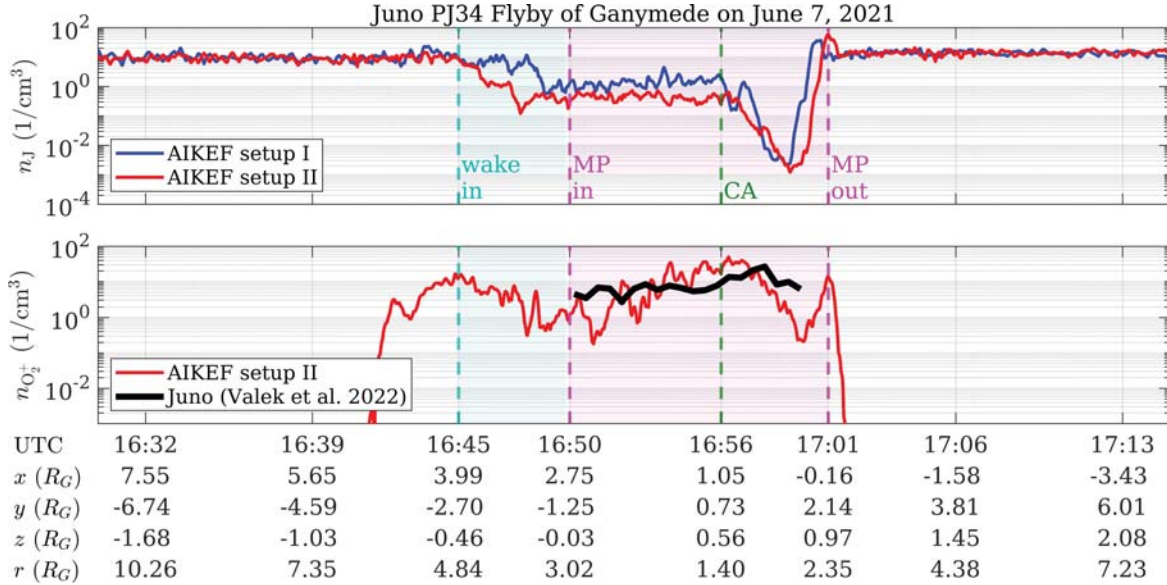


Figure 5. Juno observations and AIKEF model results of the number density of different plasma species along the PJ34 flyby trajectory of Ganymede. Panel (a) displays the number density of the Jovian plasma n_J calculated by AIKEF for both setup I (blue) and setup II (red). Panel (b) shows the O_2^+ number density $n_{O_2^+}$ observed by Juno’s JADE instrument (black, provided in Valek et al. (2022)) and produced by the AIKEF model in setup II (red). The dashed vertical lines denote the same boundaries as in Figure 3, with the teal shading corresponding to the wake region and the magenta shading to Ganymede’s magnetosphere, as identified in JADE data (Allegrini et al., 2022).

served O_2^+ number density. Panel 5(a) includes Jovian plasma density profiles along the trajectory for both setup I (blue) and setup II (red). Panel 5(b) displays the O_2^+ number density observed by Juno (black, from Valek et al., 2022) and calculated by AIKEF for model setup II (red). At the time of this writing, no time series data for the O_2^+ density collected outside of Ganymede’s magnetosphere are available in the peer-reviewed literature. Additionally, there is no time series available for the Jovian magnetospheric plasma density within Ganymede’s interaction region.

The Jovian plasma density n_J in Figure 4(c) is depleted by 1-2 orders of magnitude within Ganymede’s magnetosphere near the $z = 0$ plane and in the tail region downstream of the moon (purple regions in Figure 4(c)). The impinging plasma is largely unable to penetrate into the moon’s magnetosphere at low latitudes due to the presence

of the closed field lines, accumulating instead outside of the magnetopause while flowing toward downstream (bright yellow-orange regions in Figure 4(c)). This enhancement in Jovian ion density occurs mainly near the ramside apex and along the Jupiter-facing flank ($y > 0$) of Ganymede’s magnetopause. However, reconnection in the magnetotail occurring downstream at around $x \approx 2 R_G$ (see Figures 2(a)-(d)) accelerates a portion of the Jovian magnetospheric plasma back toward the moon. This process produces a crescent-like feature in the Jovian ion density that wraps around Ganymede’s downstream hemisphere, with values of n_J comparable to the upstream density n_0 (orange-purple crescent in Figure 4(c)). The hybrid model of Fatemi et al. (2022) shows a similar crescent pattern of enhanced Jovian ion density above the moon’s downstream hemisphere; see Figure 2(a) in that work.

In setup II, the region downstream of Ganymede becomes populated with ionospheric O_2^+ particles, comprising a pick-up tail with sharp outer flanks (orange regions in Figures 4(a) and 4(b)). The upstream magnetopause position is visible in the oxygen ion density in both the $z = 0$ and $y = 0$ planes (orange and purple border). In the same way as the Jovian magnetospheric ions, a portion of the O_2^+ ions within Ganymede’s magnetosphere are accelerated toward upstream by reconnection in the tail region. Similar to the Jovian plasma, this contributes to the formation of a crescent-like region of enhanced ionospheric O_2^+ density that wraps around Ganymede’s downstream hemisphere in the $z = 0$ plane (bright yellow-orange in Figure 4(a)). The maximum number density within this O_2^+ population occurs near the surface of the moon and is on the order of 1000 cm^{-3} . This value is only slightly lower than the maximum ionospheric electron density of 2000 cm^{-3} observed by Juno close to Ganymede’s downstream surface (Buccino et al., 2022). The value from Buccino et al. (2022) is expected to exceed that in our model since Ganymede’s actual ionosphere includes additional particle species that are not included in this AIKEF setup (Valek et al., 2022).

Some of the O_2^+ ions within the high-density crescent impinge onto the ramside magnetopause from the “inside.” In this region, the ionospheric O_2^+ is accelerated (red layer in Figure 4(e)) and diverted northward ($u_z > 0$, red in Figure 4(f)) in the $z > 0$ half space and southward ($u_z < 0$, blue in Figure 4(f)) for $z < 0$. Reconnection occurring downstream of the closed field line region ($x > 2 R_G$, see Figures 2(a)-(d)) accelerates O_2^+ ions in that region toward downstream (red and white wedge-like region in Figure 4(e)). Immediately downstream of Ganymede, the high concentration of slow O_2^+ pick-

911 up ions (blue in Figure 4(d)-(e)) reduces the convective electric field, thereby making the
 912 pick-up process less efficient. A similar “self-shielding” effect of a moon’s tail against ero-
 913 sion due to pick-up has also been described extensively for, e.g., Titan (Simon et al., 2007)
 914 and Callisto (Liuzzo et al., 2015).

915 The modeled O_2^+ velocity magnitude exhibits an asymmetry between the sub-Jovian
 916 and anti-Jovian flanks of Ganymede’s pick-up tail (see Figure 4(d)): the anti-Jovian mag-
 917 netopause flank ($y < 0$) reveals a layer up to $0.5 R_G$ thick of O_2^+ pick-up ions travel-
 918 ing at near twice the upstream bulk velocity ($2|\mathbf{u}_0|$, thin red region in Figure 4(d)). Out-
 919 side of the region of closed field lines, the O_2^+ pick-up ions gyrate largely perpendicular
 920 to the z axis and possess gyroradii of about $0.2 R_G$ (estimated using the upstream mag-
 921 netic field and velocity from Table 1). The cycloidal trajectories of these ions have “bel-
 922 lies” that extend approximately $0.4 R_G$ away from Jupiter (see Equation (30) and Fig-
 923 ure 2 of Simon et al., 2007). The Jovian plasma becomes accelerated along the outer flanks
 924 of Ganymede’s magnetosphere, thereby locally enhancing the convective electric field in
 925 these regions. The asymmetry in the cycloidal O_2^+ trajectories with respect to the di-
 926 rection of \mathbf{E}_0 (pointing into the $y < 0$ half space, see Table 1) allows the O_2^+ ions to
 927 access this region of enhanced convective field along the anti-Jovian ($y < 0$) flank, but
 928 not along the sub-Jovian ($y > 0$) flank. This results in the elevated drift velocity of these
 929 ions toward downstream on the $y < 0$ flank of Ganymede’s magnetosphere (red “ray”
 930 in Figure 4(d)). However, a similar feature is absent along the $y > 0$ flank. This idea
 931 is also supported by the time series of the modeled plasma density along Juno’s trajec-
 932 tory (see Figure 5). The O_2^+ ions “leak” out of Ganymede’s magnetosphere on the anti-
 933 Jovian flank of the pick-up tail, where they are intersected by Juno’s trajectory start-
 934 ing at about 16:42 UTC (red line in Figure 5(b)). In this region, the O_2^+ population pen-
 935 etrates into the Jovian plasma outside Ganymede’s magnetopause (red line in Figures
 936 5(a)-(b)). Near the outbound magnetopause ($y > 0$), the O_2^+ population does not sub-
 937 stantially extend outside of Ganymede’s magnetosphere along the flyby trajectory (red
 938 line in Figure 5(b)). This is consistent with Juno observations, which revealed the pres-
 939 ence of ionospheric ions within the wake region ($y < 0$), but not beyond the outbound
 940 magnetopause crossing (Allegrini et al., 2022).

941 Models of the plasma environments at Titan (e.g., Simon et al., 2007) and Cal-
 942 listo (e.g., Liuzzo et al., 2015) also display enhancements in the velocities of ionospheric
 943 pick-up ions along the planet-averted flanks of the moons’ plasma tails. However, there

944 is no magnetopause at either Titan or Callisto and therefore no boundary layer where
 945 the planetary magnetospheric plasma is prevented from substantially mixing with the
 946 ionospheric tail. The gyroradii of pick-up ions at Titan and Callisto are several times
 947 larger than the respective moon's radius (Simon et al., 2007; Liuzzo et al., 2015). As a
 948 result, the enhanced velocities of pick-up ions in the vicinities of Titan and Callisto are
 949 caused by the initial acceleration of these ions at the onset of their first "arc" of cycloidal
 950 motion. Thus, the mechanism generating the hemispheric asymmetries in pick-up ion
 951 velocities at Titan and Callisto is different from what we found at Ganymede (see Fig-
 952 ure 4(d)).

953 Both the anti-Jovian (inbound) and sub-Jovian (outbound) flanks of the modeled
 954 pick-up tail possess steep density gradients along Juno's flyby trajectory: the modeled
 955 O_2^+ number density sharply increases from near-zero to 1 cm^{-3} at about 16:42 UTC over
 956 a length scale of about $0.3 R_G$, with a comparable rate of decrease occurring near the
 957 outbound magnetopause crossing (red in Figure 5(b)). After Juno entered the pick-up
 958 tail (around 16:43 UTC), the modeled O_2^+ density builds more slowly to a maximum of
 959 about 10 cm^{-3} (near 16:45 UTC), or very close to the undisturbed upstream density n_0 .
 960 This value is consistent with the maximum "heavy" ion density of 24 cm^{-3} (which in-
 961 cludes all ion species but H^+) observed by Juno in the wake (Allegrini et al., 2022). Along
 962 Juno's trajectory, the modeled O_2^+ density within the pick-up tail then drops down to
 963 a minimum of just over 0.1 cm^{-3} at 16:48 UTC. Following this, the density slowly in-
 964 creases as the trajectory nears the Jupiter-averted magnetopause.

965 Within Ganymede's magnetosphere (magenta shading in Figure 5), the narrow range
 966 of ionospheric O_2^+ densities observed by Juno largely agrees with the AIKEF results for
 967 setup II (red versus black lines in Figure 5(b)). Both the model results and the observed
 968 O_2^+ number density gradually increase inside the moon's magnetosphere from about 2
 969 cm^{-3} (model) and 4 cm^{-3} (observations) to comparable maximums near closest approach:
 970 the modeled ionospheric O_2^+ population reaches a peak density of about 50 cm^{-3} just
 971 after 16:56 UTC, which agrees reasonably well with the observed maximum of 30 cm^{-3} .
 972 However, while the modeled peak in O_2^+ number density occurs about 30 seconds after
 973 closest approach, the observed peak in this value was detected by Juno 2 minutes after
 974 closest approach (see Figure 5(b)). The location and magnitude of the peak O_2^+ density
 975 in our model are also similar to those of the peak in electron density observed by the Waves
 976 instrument (Kurth et al., 2022, see their Figure 2). Shortly after the observed time se-

ries from Valek et al. (2022) ends (16:59 UTC), the modeled O_2^+ pick-up ion density briefly spikes to about 10 cm^{-3} . This feature reflects the accumulation of ionospheric ions inside of Ganymede's magnetopause (also visible in Figure 4(a)). The O_2^+ density largely disappears outbound of Ganymede's Jupiter-facing magnetopause, falling by over three orders of magnitude near the boundary layer (red lines in Figures 5(a)-(b)).

Both setup I and setup II display a reduced Jovian magnetospheric ion density within the wake region and an even stronger decrease inside of Ganymede's magnetosphere (see Figure 5(a)). However, while the upstream density in setup I (blue) does not significantly drop until after $1.0 R_G$ into the wake region (16:48 UTC), the density in setup II (red) begins to decrease as soon as the trajectory intersects the wake (16:45 UTC). In setup II, the Jovian ion density within the wake falls by over two orders of magnitude to a minimum of around 0.05 cm^{-3} at 16:48 UTC. This again contrasts with setup I, which displays a less pronounced minimum of about 1 cm^{-3} in the wake region, occurring much closer to the inbound magnetopause crossing at 16:50 UTC (blue in Figure 5(a)). The stronger density decrease in setup II is caused by the ionospheric plasma pushing the Jovian plasma out of the region populated by O_2^+ ions through the pressure gradient forces at the steep outer flanks of the pick-up tail. Inside of Ganymede's magnetosphere, the Jovian ion density along the flyby trajectory remains a factor of 3-4 lower in setup II than in setup I. After closest approach, this value is further reduced to a minimum of about 10^{-3} cm^{-3} in both model setups. Following this drop, the Jovian ion density abruptly increases to near the background value at the outbound magnetopause crossing (about 17:00 UTC, see Figure 5(a)).

Figure 6(a) displays the magnetic field components observed along Juno's trajectory (black), the model results from setup II (red), and the output of the vacuum superposition model (blue). Figure 6(b) again features B_z , but zoomed in over the short segment of the trajectory centered around the observed outbound magnetopause crossing, and plotted versus r rather than time. The line labeled t_0 (light pink) corresponds to an arbitrary starting point in the time *after* the upstream flow has completed a full passage through the model domain and the large-scale features of the interaction (e.g., the OCFB) have reached a quasi-stationary state. The other lines represent “snapshots” of the modeled B_z component at times $t_0 < t_1 < t_2 \dots < t_5$, taken in increments of 54 seconds (starting at t_0). The increment between consecutive B_z snapshots corresponds to the time required by the Jovian plasma to travel about $2.7 R_G$, or about half the span

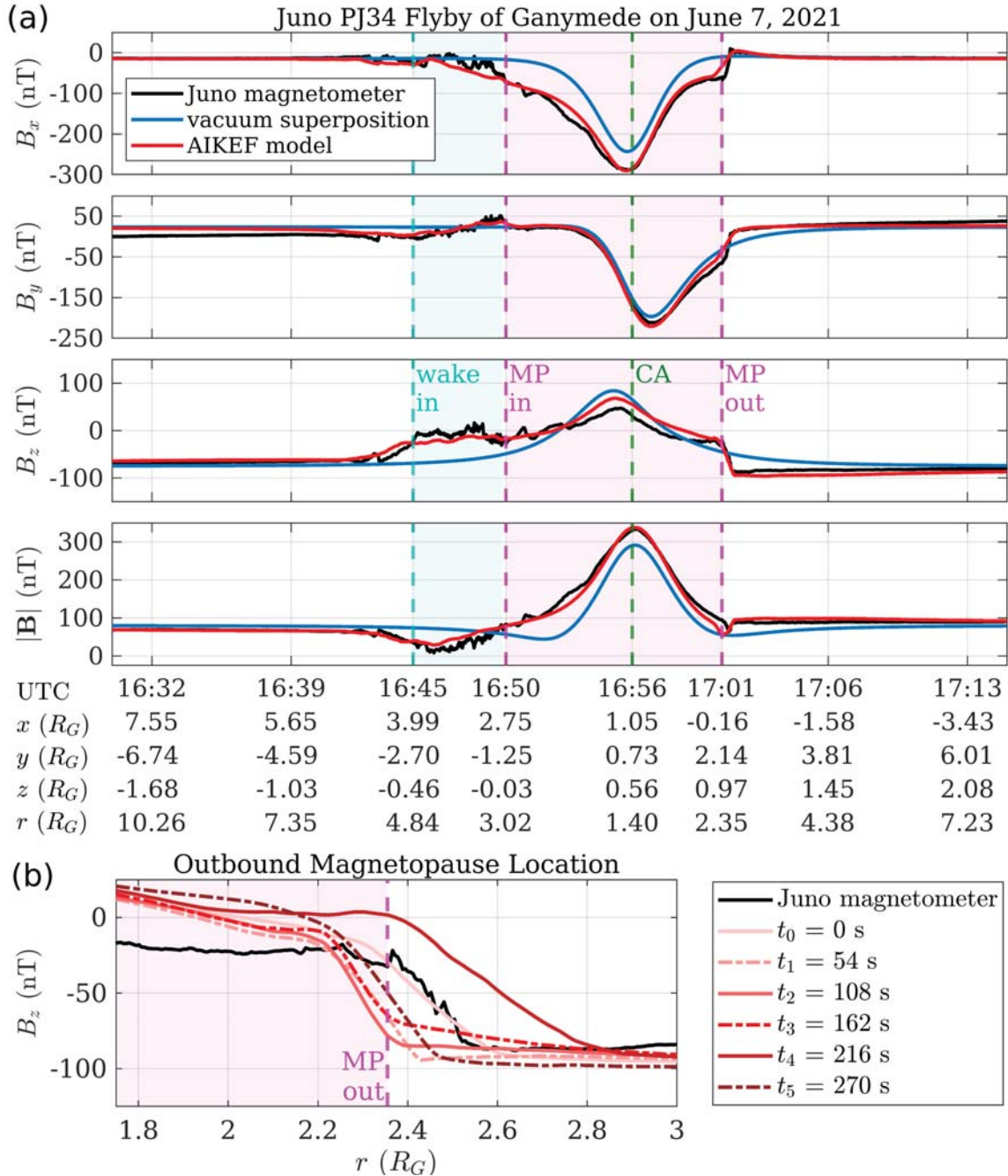


Figure 6. Comparison of modeled and observed magnetic field for setup II. Panel (a) displays time series of Juno magnetometer data, setup II results, and the output of the vacuum superposition model along the flyby trajectory. The layout is the same as in Figure 3, with B_x , B_y , B_z , and $|B|$ arranged from top-to-bottom. The vertical dashed lines again indicate the boundaries between different sectors of Ganymede's interaction region. The teal and magenta shading correspond to the wake region and the moon's magnetosphere, respectively. Panel (b) displays the observed (black line) and modeled (colored lines) B_z component, zoomed-in about the observed outbound magnetopause crossing. All modeled results in panel (b) are obtained from setup II. The model result at time $t = t_0$ (light pink line) represents an arbitrary point in time *after* the large-scale features in the AIKEF model have reached a quasi-stationary state and the upstream plasma has completed at least one full crossing of the model domain. This time (t_0) also corresponds to the modeled magnetic field results in panel (a). The other colored lines represent the modeled B_z component at later points in time ($t_1 < t_2 \dots < t_5$), each of them separated by 54 seconds from the previous and the lines becoming increasingly darker as time progresses. This spacing corresponds to the time required for the upstream plasma to travel about $2.7 R_G$ in the $+x$ direction. The illustration in panel (b) indicates how the location of the modeled outbound magnetopause crossing along the flyby trajectory varies in time.

of Ganymede's closed field line region along the x axis near the $z = 0$ plane. This "flip-book" reveals the time variability in the location of the outbound magnetopause along Juno's trajectory (see Figure 2(a)).

While the inclusion of the O_2^+ ionosphere produces quantitative changes to the modeled magnetic field signature near Ganymede, it has minimal *qualitative* impact on the moon's magnetic environment. When the O_2^+ ions are picked-up by the impinging Jovian magnetospheric plasma, they further decelerate the flow and bend the Jovian field lines, in addition to the bending caused by Ganymede's internal field (e.g., Neubauer, 1999). Along Juno's trajectory, this effect amplifies the reduction to B_x from field line draping seen in setup I: inside Ganymede's magnetosphere, the modeled B_x in setup II more closely matches the observed values and deviates from the minimum by only about 1 nT compared to 15 nT in setup I (Figure 3 and top panel in Figure 6(a)). The ionospheric O_2^+ also increases the effective size of the obstacle to the impinging flow. Within the wake region, the B_x component in setup II therefore drops slightly below the observed values. In contrast to this, the modeled and observed B_x signatures within the wake were almost indistinguishable in setup I.

The magnetic field perturbations near closest approach are dominated by B_x , which therefore also leaves the strongest imprint on the field magnitude $|\mathbf{B}|$ in the immediate vicinity of Ganymede. Within the moon's magnetosphere, the inbound and outbound flanks of the modeled $|\mathbf{B}|$ enhancement in setup II thus better match the observed values. The maximum of the modeled $|\mathbf{B}|$ in setup II falls within only ~ 1 nT of the observed maximum, with both of them occurring shortly after closest approach at about 16:56:30 UTC (Figure 6(a)). The modeled B_y component does not display meaningful differences between setups I and II: the time series from both AIKEF setups reveals minimal perturbations from plasma currents and largely overlaps with both the Juno observations and the vacuum superposition model. The B_z component in setup II exhibits slightly enhanced perturbations in the wake region by about 10 nT compared to setup I, approximately matching Juno observations as the spacecraft approached Ganymede's inbound magnetopause.

In model setup I, the outbound magnetopause crossing was located about $\Delta x = 0.2 R_G$ farther downstream and $\Delta r = -0.2 R_G$ closer to Ganymede than was observed by Juno (see Figure 3). However, in model setup II, increased counter-pressure from iono-

1042 spheric O_2^+ inside of Ganymede's magnetosphere pushes the modeled magnetopause far-
 1043 ther away from the moon. This causes the location of the modeled outbound magnetopause
 1044 crossing to shift to a slightly later point in time (+1 minute) and farther from the moon
 1045 ($\Delta r \approx +0.2 R_G$) along the trajectory when compared to setup I. As can be seen from
 1046 the modeled B_x and B_z components in Figure 6(a), the modeled outbound magnetopause
 1047 location demonstrates substantially better agreement with Juno observations in setup
 1048 II. However, the presence of the O_2^+ ionosphere also introduces an additional *time vari-*
 1049 *ability* to the outbound magnetopause location and the corresponding jumps in the B_x
 1050 and B_z components. As displayed in Figure 6(b) for the B_z component, the location of
 1051 the modeled outbound magnetopause crossing varies by $\Delta r \approx \pm 0.15 R_G$ on time scales
 1052 of about one minute. Hence, the modeled location of the anti-Jovian magnetopause seen
 1053 in Figure 6(a) merely represents a snapshot in time: the position of the modeled mag-
 1054 netopause crossing along Juno's trajectory continuously evolves as the incident plasma
 1055 flows past the moon. The length scales of this variability are small compared to the over-
 1056 all size of Ganymede's magnetosphere. However, the uncertainty in the location of the
 1057 *observed* outbound magnetopause crossing associated with this effect is significant: had
 1058 Juno sampled the outbound magnetopause a minute earlier or later under identical am-
 1059 bient plasma conditions, our setup II results suggest that the crossing of this boundary
 1060 layer would have been detected at a location up to $0.15 R_G$ closer to Ganymede or 0.15
 1061 R_G farther away from the moon.

1062 The time-variability in the location of Ganymede's Jupiter-facing magnetopause
 1063 in setup II is caused by Kelvin-Helmholtz instability (KHI) propagating along this bound-
 1064 ary. This instability forms as a result of shear flow between the dense O_2^+ populating Ganymede's
 1065 magnetosphere and the adjacent flow from Jupiter's magnetosphere. We note that the
 1066 KHI also manifests in setup I in the same region of the magnetopause (Jupiter-facing
 1067 flank, $y > 0$). In that setup, it arises from velocity shear between the flow outside of
 1068 Ganymede's magnetopause and the Jovian magnetospheric plasma that populates the
 1069 moon's mini-magnetosphere and is accelerated toward upstream by reconnection in the
 1070 tail region (see also Kaweeyanun et al., 2021). However, perturbations from the KHI in
 1071 setup I are much weaker than in any of our four setups (II-V) which include an ionosphere,
 1072 and the resulting spatial variability of the outbound magnetopause location along Juno's
 1073 trajectory is on the order of the grid resolution in AIKEF.

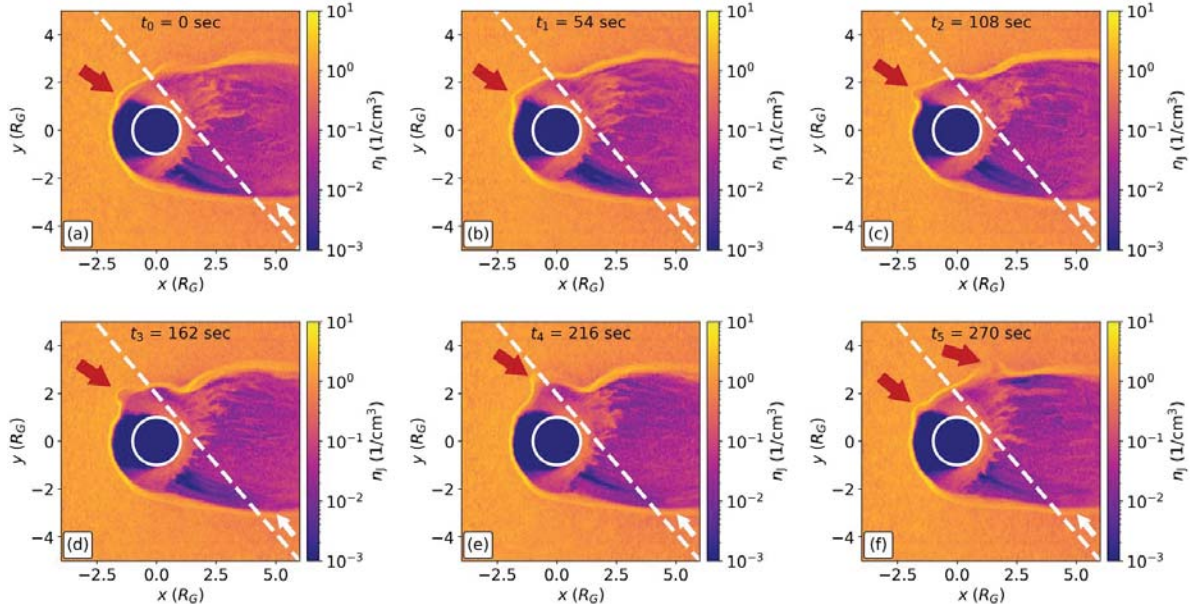


Figure 7. AIKEF results of the Kelvin-Helmholtz instability (KHI) as seen in the Jovian plasma density of setup II. All panels provide two-dimensional color plots of the Jovian ion number density n_J in the $z = 0$ plane. The red arrow in each panel identifies the KHI perturbation traveling along the sub-Jovian magnetopause flank, with the final panel including an additional arrow (on the left) to identify a second, subsequent KHI perturbation. Panel (a) corresponds to an arbitrarily chosen “start” time after the large-scale features in the model output have reached a quasi-stationary state. Each subsequent panel (b)-(f) advances the time by 54 seconds, with 270 seconds having elapsed in the final panel of the sequence (f). The points in time chosen to generate this illustration are the same as in Figure 6(b). Juno’s flyby trajectory is indicated by the dashed white line and the accompanying white arrow corresponds to the spacecraft’s direction. Ganymede is identified by the white circle of radius $1 R_G$ centered on the origin.

1074 Figure 7 displays a “flip-book” of the time evolution of the KHI in setup II, pro-
 1075 viding two-dimensional context for the time variability of the sub-Jovian magnetopause
 1076 location along Juno’s trajectory. Each panel shows a snapshot in time of the Jovian plasma
 1077 density in the $z = 0$ plane. The points in time ($t = t_0, \dots, t_5$) sampled in Figure 7 are
 1078 the same as indicated in Figure 6(b). Ganymede’s magnetopause is located at the bound-
 1079 ary between the low density (dark orange and purple) and background density (bright
 1080 yellow-orange) regions in Figure 7, with the KHI appearing on the sub-Jovian ($y > 0$)
 1081 flank of this boundary and indicated by the red arrows in each panel. The final panel

1082 (f) includes a second arrow (on the left) to indicate the beginning growth of a subsequent
 1083 KHI perturbation.

1084 In the snapshot at time $t = t_0$, a small wave-like perturbation starts to form in
 1085 the $y > 0$ segment of the upstream magnetopause, as identified by the red arrow in Fig-
 1086 ure 7(a). Subsequently, this perturbation grows in amplitude and is gradually acceler-
 1087 ated along the Jupiter-facing magnetopause flank (Figures 7(b)-(c)). The KH wave then
 1088 approaches Juno's intersection with the sub-Jovian magnetopause flank, causing the lo-
 1089 cation of the outbound magnetopause near the trajectory to be first pulled toward the
 1090 moon by $\Delta r \approx -0.15 R_G$ (Figures 7(b)-(d), see also times t_1-t_3 in Figure 6(b)), and
 1091 then pushed out by up to $\Delta r \approx 0.15 R_G$ (Figure 7(e), see also time t_4 in Figure 6(b)).
 1092 After this, the magnetopause retracts to just inside of the observed location again (Fig-
 1093 ure 7(f), see also time t_5 in Figure 6(b)). The modeled KH waves propagate toward down-
 1094 stream at 30-50 km/s, or up to approximately one-third of the upstream plasma bulk
 1095 velocity $|\mathbf{u}_0|$. Consecutive KHI bulges form at the Jupiter-facing ($y > 0$), upstream face
 1096 of the magnetopause in time increments of just under 5 minutes: the next KH bulge can
 1097 be seen forming at the same location as the first one at time t_5 (red arrow on left in Fig-
 1098 ure 7(f)).

1099 The population of O_2^+ ions that “leak” out of the Jupiter-averted magnetopause
 1100 flank (Figure 5, and hazy purple in Figure 4(a)) move toward downstream at velocities
 1101 comparable to the bulk velocity $|\mathbf{u}_0|$ of the upstream plasma flowing around the mag-
 1102 netosphere (red in Figure 4(d)). This high O_2^+ velocity reduces the shear between Ganymede's
 1103 ionospheric and Jupiter's magnetospheric flow, thereby suppressing the KHI formation
 1104 along the Jupiter-averted magnetopause ($y < 0$). Due to the orientation of their cy-
 1105 cloidal trajectories, O_2^+ pick-up ions remain inside of Ganymede's magnetosphere near
 1106 the Jupiter-facing magnetopause flank (see Figures 4(a) and 4(d)). Therefore, the elec-
 1107 tromagnetic fields in the adjacent Jovian flow are unable to enhance the drift velocity
 1108 of these ions, thereby generating a velocity gradient across the magnetopause that makes
 1109 it susceptible to KHI growth. The asymmetric KHI formation in our model agrees with
 1110 the analytical work of Kaweeyanun et al. (2021), who also suggested suppression of the
 1111 KHI along the $y < 0$ magnetopause. However, the analytical calculations by these au-
 1112 thors do not take into account any pick-up ions from Ganymede's ionosphere, and the
 1113 asymmetry in KHI formation is explained solely through the opposite sense of ion gy-

ration in Ganymede's equatorial magnetic field, compared to the sense in the ambient Jovian field (see Figure 4(a) of that work).

3.3 Setups III, IV, and V: Inclusion of H₂ and H₂O Atmospheres

In this section, we present the model results for setups III, IV, and V, each of which adds an additional element of complexity to Ganymede's atmosphere and/or ionosphere (see Table 2). These model configurations utilize the same parameters for the upstream plasma and Ganymede's internal field as setups I and II. In setup III, a symmetric H₂ atmosphere is included (in addition to the O₂ atmosphere), and Ganymede's neutral envelope is exposed to uniform electron impact ionization. Setup IV adds dayside photo-ionization to both O₂ and H₂. Finally, setup V adds an atmospheric H₂O "bulge" centered about the subsolar point (see Section 2.3). This water component is again exposed to uniform electron impact ionization and dayside photo-ionization.

In Figure 8, we display two-dimensional color plots of the modeled ion density for all three ionospheric species (panels (a)-(g)), as well as the H₂⁺ bulk velocity (panels (h)-(j)). The three columns correspond to setups III (left), IV (middle), and V (right). Figure 9 displays the time series along Juno's flyby trajectory for the observed and modeled number densities of O₂⁺ (panel (a)) and H₂⁺ (panel (b)). Again, time series of observed ion densities are available only for the segment of the trajectory inside of Ganymede's magnetosphere (16:50 UTC to 16:59 UTC, see Valek et al. (2022)). Across all setups, the modeled H₂⁺ densities along the trajectory display excellent quantitative agreement with Juno observations from Valek et al. (2022); see Figure 9(b). For O₂⁺, the inclusion of additional ionospheric components in setups III-V does not affect the agreement between the modeled and observed time series, compared to setup II (see Section 3.2 and Figure 9(a)).

The modeled ionospheric O₂⁺ density patterns in the $z = 0$ plane are qualitatively similar across setups III-V (top row in Figure 8). Inside of Ganymede's magnetosphere and pick-up tail, the O₂⁺ density in these setups show only minor quantitative differences from those in the output of setup II (see Figure 4(a)). The modeled O₂⁺ density along the flyby trajectory confirms minimal qualitative differences between this quantity in setups II-V (see Figure 9(a)). Compared to model setup II, the O₂⁺ pick-up tail in setups III-V (Figures 8(a)-(c)) is slightly narrower perpendicular to the x direction at interme-

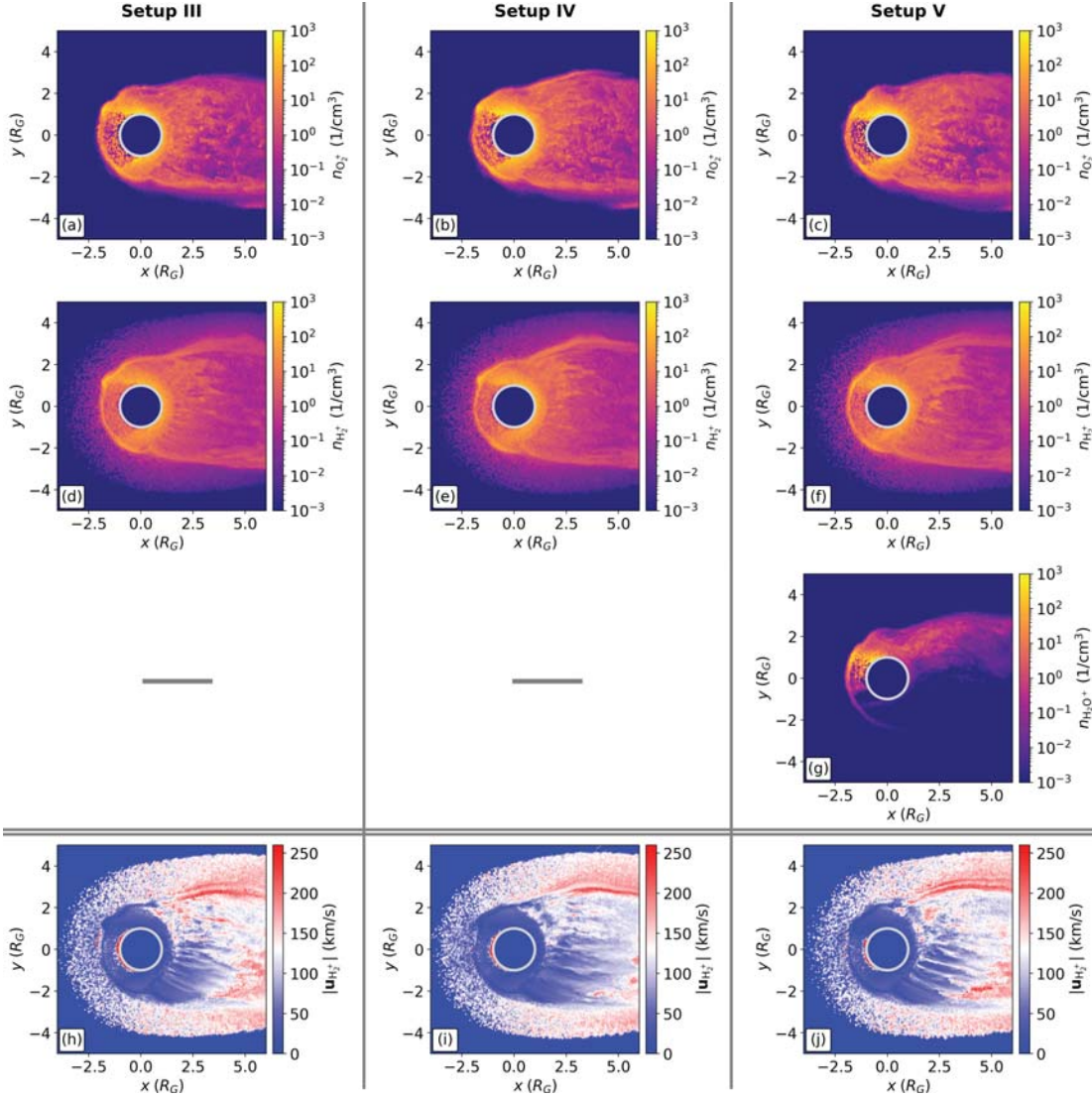


Figure 8. Two-dimensional color plots of the modeled ionospheric densities and H_2^+ bulk flow velocity for setups III, IV, and V (see Section 2.3). Setup III includes a symmetric O_2 and H_2 atmosphere and exposes both species to uniform electron impact ionization. Setup IV then adds dayside photo-ionization of both O_2 and H_2 . Finally, an H_2O atmospheric bulge centered about the subsolar point (see Figure 1) is added in setup V, with all three neutral species subjected to uniform electron impact ionization and dayside photo-ionization. The figure includes: (a)-(c) ionospheric O_2^+ number density $n_{\text{O}_2^+}$, (d)-(f) ionospheric H_2^+ number density $n_{\text{H}_2^+}$, (g) ionospheric H_2O^+ number density $n_{\text{H}_2\text{O}^+}$, and (h)-(j) the magnitude of the H_2^+ bulk velocity $|\mathbf{u}_{\text{H}_2^+}|$. All plots are in the $z = 0$ plane, with Ganymede indicated by the light gray circle of radius $1 R_G$ centered at the origin. The columns correspond to setups III (left), IV (middle), and V (right). Because setup V is the only one containing H_2O^+ ions, only a single panel is shown in the third row of the figure.

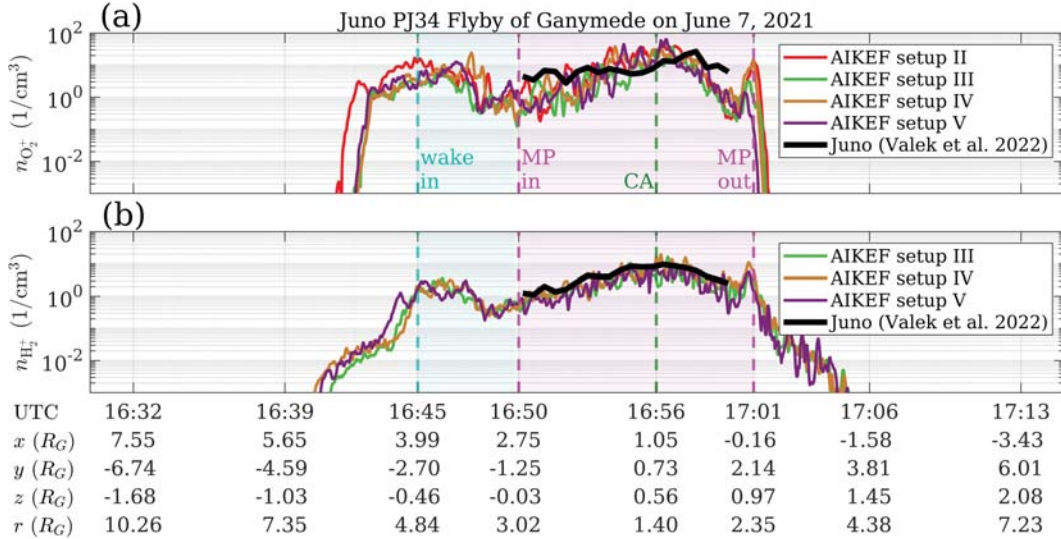


Figure 9. Juno observations and AIKEF model results for the number densities of ionospheric O_2^+ and H_2^+ ions along the PJ34 flyby trajectory. Panel (a) displays the number density of O_2^+ ions observed by Juno (black, provided in Valek et al. (2022)) and produced by the AIKEF model in setups II (red), III (green), IV (brown), and V (purple). The O_2^+ densities from setup II are the same as in Figure 5(b), but we show them again here to facilitate comparison to the more complex ionosphere models. Panel (b) displays the H_2^+ number density observed by Juno (black) and produced by AIKEF for setups III (green), IV (brown), and V (purple). Since the hydrogen component of Ganymede's atmosphere is not included in setup II, the figure does not include a modeled time series of $n_{H_2^+}$ from setup II. The dashed vertical lines denote the same plasma boundaries as in Figures 3, 5, and 6. Teal shading indicates the segment of the trajectory inside of the wake region and magenta shading indicates the portion of the trajectory within Ganymede's magnetosphere, according to Juno JADE data (Allegrini et al., 2022).

diate distances to Ganymede ($x \approx 1.5R_G$). This is also visible along Juno's trajectory in Figure 9(a): the inbound segment of the flyby trajectory intersects the modeled O_2^+ population about $0.15 R_G$ farther outside the wake region in setup II (red) than in setups III-V (green, brown, purple).

Because the O_2^+ number density is comparable to that of H_2^+ throughout Ganymede's magnetosphere (see Figures 8(a)-(f) and 9(a)-(b)), the heavier O_2^+ ions drain a much greater amount of the momentum from the impinging Jovian flow. The H_2^+ mass density outside of the moon's magnetosphere (where no O_2^+ is present) is exceeded by that of the

1153 Jovian plasma by at least three orders of magnitude. Thus, mass loading of the Jovian
 1154 plasma by H_2^+ ions outside of Ganymede's magnetosphere does not appreciably decel-
 1155 erate the flow. In consequence, the light H_2^+ ions included in setups III-V can be con-
 1156 sidered as test particles throughout Ganymede's interaction region, i.e., they do not sub-
 1157 stantively affect the structure of the O_2^+ pick-up tail (see Figures 8(a)-(c)). An analo-
 1158 gous behavior was found for the light hydrogen ions populating Titan's interaction re-
 1159 gion (e.g., see Simon et al., 2007). In setups III-V, a crescent of elevated H_2^+ density forms
 1160 around Ganymede's downstream hemisphere (yellow in Figures 8(d)-(f)) and largely over-
 1161 laps with the high-density crescent of O_2^+ ions (yellow in Figures 4(a) and 8(a)-(c)). The
 1162 H_2^+ crescent extends to the upstream magnetopause in both hemispheres. As displayed
 1163 by the O_2^+ and H_2^+ densities in Figures 8(a)-(f), there are again KH waves visible on the
 1164 Jupiter-facing magnetopause flank in setups III-V. The amplitudes and propagation ve-
 1165 locities of these waves are similar to those produced in setup II (see Figure 7).

1166 The atmospheric scale height of H_2 ($0.38 R_G$ in our model, see Section 2.3) is four
 1167 times greater than that of O_2 and only about a factor of two smaller than the ramside
 1168 stand-off distance of Ganymede's magnetopause ($0.9 R_G$, see Figures 2(b) and 4). As
 1169 a result, a dilute envelope of H_2 surrounds Ganymede's magnetosphere. The associated
 1170 H_2^+ ions form a symmetric "corona" *outside* of the magnetopause (hazy purple in Fig-
 1171 ures 8(d)-(f)). Along the Juno trajectory, the region populated by H_2^+ is more extended
 1172 (by about $0.6 R_G$ inbound and $1.3 R_G$ outbound) than the O_2^+ tail (Figures 9(a)-(b)).
 1173 Consistent with these modeling results, Juno detected the presence of H_2^+ ions just prior
 1174 to entering and after exiting Ganymede's magnetosphere. These detections occurred be-
 1175 fore (inbound) and after (outbound) O_2^+ was encountered along the trajectory (Allegrini
 1176 et al., 2022). The H_2^+ ions produced outside of the moon's magnetosphere are picked up
 1177 and carried toward downstream along the outer flanks of the magnetopause at speeds
 1178 near the upstream bulk velocity $|\mathbf{u}_0|$ (white and red in Figures 8(h)-(j)). The inclusion
 1179 of photo-ionization (setup IV) and the additional H_2O^+ component (setup V) have min-
 1180 imal quantitative impact on the bulk velocity of H_2^+ in Ganymede's interaction region.

1181 Our model results show that the H_2^+ ions populate the wake region along the Jupiter-
 1182 averted magnetopause flank at densities of up to about $0.5 n_0$ (Figures 8(d)-(f) and 9(b)).
 1183 Just outside the Jupiter-averted edge of the wake, the H_2^+ density falls sharply to be-
 1184 low $10^{-3} n_0$ in all setups (16:44 UTC to 16:45 UTC in Figure 9(b)). In contrast to this,
 1185 the modeled O_2^+ in Ganymede's Jupiter-averted hemisphere maintains densities of about

1186 n_0 (between 16:42 UTC and 16:45 UTC in Figure 9(a)). The observed time series and
 1187 model results for setups III-V all reveal a maximum H_2^+ density along the trajectory of
 1188 about 10 cm^{-3} ($\approx n_0$), occurring near closest approach. After the observed time series
 1189 ends, the H_2^+ population displays a similar behavior as O_2^+ : a local minimum in H_2^+ den-
 1190 sity occurs at 17:00 UTC, followed by an enhancement just before the outbound mag-
 1191 netopause crossing (Figure 9(b)).

1192 A comparison of the ion number densities between setups III and IV (Figures 8(a)
 1193 and 8(d) versus 8(b) and 8(e)) illustrates that the inclusion of dayside photo-ionization
 1194 has only very minor quantitative impact on the tail structure of the O_2^+ and H_2^+ ions.
 1195 The modeled ion densities along Juno's trajectory in Figures 9(a) and 9(b) also indicate
 1196 no discernible difference between setups III (green) and IV (brown) due to photo-ionization.
 1197 This similarity stems from the small ratios of photo-ionization to electron impact ion-
 1198 ization rates at Ganymede, which are about 0.3 for O_2^+ and 0.05 for H_2^+ (see Table 2).
 1199 In model setup V, production of H_2O^+ ions is confined to the low-latitude region around
 1200 the subsolar point in the Jupiter-facing, upstream hemisphere (see Figure 1). The H_2O
 1201 component of Ganymede's atmosphere has a scale height of only $0.08 R_G$ (see Section
 1202 2.3). Therefore, most H_2O^+ ions are generated inside the closed field line region, which
 1203 near the $z = 0$ plane extends from Ganymede's surface about $0.9 R_G$ toward upstream
 1204 and $1.0 R_G$ into the Jupiter-facing and Jupiter-averted half spaces (see Figures 2(a)-(c)
 1205 and 2(g)-(i)). As a result, the bulk of the newly generated H_2O^+ ions are unable to "break
 1206 free" of the closed magnetic field lines and do not contribute to the formation of the moon's
 1207 pick-up tail.

1208 The dilute H_2O^+ pick-up tail that is still formed resides in the $y > 0$ half space
 1209 due to the location of the subsolar point in the Jupiter-facing hemisphere during PJ34
 1210 (Figures 1 and 8(g)). The H_2O^+ tail displays peak densities of only about 0.5 cm^{-3} . Al-
 1211 though H_2O possesses a similar neutral column density and production rate to O_2 , this
 1212 is over an order of magnitude lower than for O_2^+ in the same region. The low density of
 1213 H_2O^+ pick-up ions in Ganymede's tail agrees with observations, which place an upper
 1214 limit of less than a few percent on the contribution of H_2O^+ to the total ion mass den-
 1215 sity detected by Juno's JADE instrument (Valek et al., 2022). In reality, the H_2O bulge
 1216 about the subsolar point is suggested to have a smaller scale height (about 50 km, see
 1217 e.g., Vorburger et al., 2022) than assumed by our model. Production of H_2O^+ would there-
 1218 fore be even more confined (in the radial direction), compared to the radial extension

of the closed field line region. As a result, an even larger fraction of the H_2O^+ ions would remain “trapped” near Ganymede, and the H_2O^+ number density in the pick-up tail would be even lower than shown in Figure 8(g). The confinement of escaping ions of a certain species to a narrow outflow channel has been observed by the Cassini spacecraft during its wakeside T9, T63, and T75 flybys of Titan (Szego et al., 2007; Coates et al., 2012). However, at Titan, such channels were populated only by ions of a single mass-to-charge ratio. In contrast to this, our results for Ganymede suggest that the tail “ray” formed by the H_2O^+ ions still overlaps with the much broader tails formed by O_2^+ and H_2^+ ions.

In setups III-V, the O_2^+ ions dominate the ionospheric outflow, with approximately 10^{27} ions per second (53 kg/s) exiting the model domain at its downstream face. The modeled pick-up rates of the two minor species, H_2^+ and H_2O^+ , are about 10^{26} and 10^{24} ions per second, respectively, corresponding to 0.3 kg/s and 0.03 kg/s. Paty et al. (2008) constrained ionospheric outflow at Ganymede using a multi-fluid model that included an ionosphere composed of the atomic O^+ and H^+ ions (compared to our choice of molecular ionospheric constituents). These authors estimated a total loss rate (for both ionospheric species combined) of 10^{26} ions per second. Hence, their value is about an order of magnitude lower than suggested by our model. This discrepancy may result from these authors’ choice of 125 km for the scale height of both ionospheric species, which corresponds to approximately 0.5 and 0.125 of the atmospheric scale heights used in our model for O_2^+ and H_2^+ , respectively. A smaller scale height causes a greater proportion of ion production to take place inside of Ganymede’s closed field line region, thereby reducing the fraction of ionospheric particles able to escape toward downstream.

Figure 10 displays the magnetic field components observed along Juno’s trajectory (black) and the model results from setups II (red), III (green), IV (brown), and V (purple). Increasing the complexity of Ganymede’s atmosphere and ionosphere (setups III-V) does not produce any substantial differences in the modeled magnetic field signature compared to setup II, which considers only ionospheric O_2^+ ions. In general, the four model setups which include an ionosphere around Ganymede can quantitatively reproduce all key features of the Juno magnetometer observations. This suggests that for wakeside flybys at intermediate distance, the observable magnetic signature is largely determined by the interaction between Ganymede’s internal dipole and the impinging Jovian magnetospheric plasma (see setup I). However, the addition of an O_2^+ ionosphere slightly inflates the moon’s magnetosphere, thereby improving agreement between the modeled and

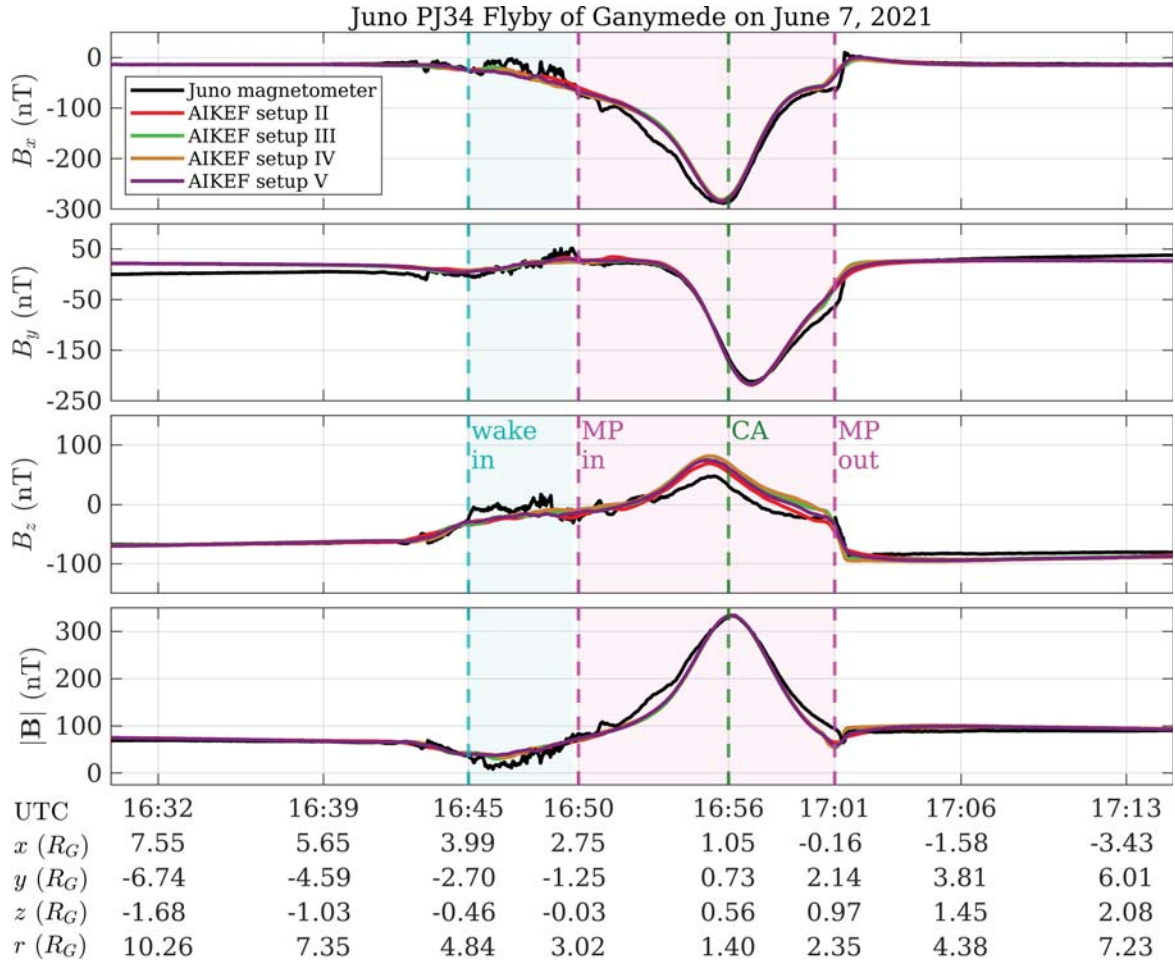


Figure 10. Comparison of the magnetic field components observed by Juno (black) and the AIKEF results for model setups II (red), III (green), IV (brown), and V (purple) along the PJ34 flyby trajectory. The layout is the same as in Figure 3, with B_x , B_y , B_z , and $|\mathbf{B}|$ arranged from top-to-bottom. The vertical dashed lines and background shading again correspond to boundaries between different regimes of Ganymede’s interaction region. Results from setup II are shown here again to facilitate comparison with output from the configurations using more complex ionosphere models.

observed magnetic field. Adding the light H_2^+ ions (which behave like test particles) or the highly localized H_2O^+ bulge does not have a discernible impact on the modeled magnetic field downstream of Ganymede. Hence, the magnetic field signature observed during the Juno flyby is not suitable to indirectly “measure” the complexity of Ganymede’s ionosphere. Such an attempt would have been feasible only if ion cyclotron waves had

been detected during the encounter (at the gyrofrequencies of the respective ion species).

However, such waves may only reach detectable amplitudes much farther downstream.

4 Conclusion

In this study, we have analyzed Ganymede's magnetic and plasma environment during Juno's PJ34 flyby on 7 June 2021. To accomplish this, we employed the AIKEF hybrid (kinetic ions, fluid electrons) plasma model (Müller et al., 2011), using upstream conditions consistent with those observed during the Juno flyby (e.g., Hansen et al., 2022; Weber et al., 2022; Allegrini et al., 2022; Kurth et al., 2022). Five ionosphere models of increasing complexity were evaluated, starting from a “baseline” case with no ionosphere at all (setup I). We then introduced a symmetric O₂ atmosphere around Ganymede (setup II), followed by symmetric O₂ and H₂ atmospheres within the same model run (setup III). In these two setups, uniform electron impact ionization was applied to Ganymede's neutral envelope. Dayside photo-ionization of both O₂ and H₂ was then added in setup IV. Finally, an atmospheric H₂O bulge centered about the subsolar point (e.g., Leblanc et al., 2023) was added, and all three constituents were exposed to both uniform electron impact ionization and dayside photo-ionization (setup V). We analyzed how the varying ionosphere configurations affect the magnetic field perturbations in Ganymede's interaction region. We also studied the dynamics of each ion species in the moon's magnetosphere and pick-up tail.

Our major results are as follows:

1. The magnetic field perturbations observed along Juno's flyby trajectory are dominated by Ganymede's internal dipole and its interaction with the impinging Jovian magnetospheric flow. The magnetic perturbations are dominated by plasma currents only within the observed “wake” region (Allegrini et al., 2022). Regardless of the chosen level of complexity, Ganymede's ionosphere produces only subtle signatures in the magnetic field along Juno's trajectory.
2. The O₂⁺ pick-up ions populate the region dominated by Ganymede's internal field and form a tail with steep boundaries along its Jupiter-facing and Jupiter-averted flanks. The O₂⁺ ions are only able to penetrate the moon's Jupiter-averted ($y < 0$) magnetopause due to their large gyroradii (about 0.2 R_G).

- 1287 3. Flow shear between ionospheric O_2^+ ions and the Jovian magnetospheric plasma
 1288 generates signatures of Kelvin-Helmholtz instability (KHI) along the Jupiter-facing
 1289 ($y > 0$) flank of Ganymede's magnetopause. The KHI introduces quasi-periodic
 1290 “breathing” of the Jupiter-facing magnetopause location, which moves in and out
 1291 from Ganymede by about $0.15 R_G$ over a period of approximately 5 minutes. In
 1292 the outbound segment of Juno's flyby, the spacecraft passed through this region
 1293 affected by KHI, indicating that the observed magnetopause crossing only provides
 1294 a snapshot in time of the Jupiter-facing magnetopause location. Had the flyby oc-
 1295 curred a few minutes earlier or later, our results suggest that the outbound mag-
 1296 netopause crossing may have been offset by up to $0.15 R_G$ in either direction along
 1297 the trajectory.
- 1298 4. Due to the large scale height of atmospheric H_2 (about $0.4 R_G$), a significant amount
 1299 of H_2^+ ions are produced outside of Ganymede's magnetopause. These ions form
 1300 a dilute “corona” around the moon's magnetosphere. The inclusion of H_2 (setup
 1301 III), dayside photo-ionization (setup IV), and H_2O (setup V) all yield only min-
 1302 imal quantitative changes in the structure of Ganymede's magnetosphere and plasma
 1303 tail. The modeled O_2^+ and H_2^+ densities both closely match the time series observed
 1304 by Juno's JADE instrument within Ganymede's magnetosphere.
- 1305 5. Ganymede's H_2O^+ pick-up tail is very dilute, possessing number densities two or-
 1306 ders of magnitude below those of the O_2^+ tail. Due to the small scale height of H_2O
 1307 and the location of Ganymede's subsolar point in the equatorial plane (about which
 1308 the H_2O bulge is centered), most of the H_2O^+ ion production occurs within the
 1309 closed field line region. Such ions are mostly unable to escape toward downstream
 1310 and therefore cannot contribute to the moon's pick-up tail.
- 1311 6. In our model, the total ionospheric outflow is dominated by O_2^+ , with approximately
 1312 $10^{27} O_2^+$ ions/s (53 kg/s) escaping Ganymede's magnetosphere. The outflow rates
 1313 are about 10^{26} ions/s (0.3 kg/s) and 10^{24} ions/s (0.03 kg/s) for ionospheric H_2^+
 1314 and H_2O^+ , respectively.

1315 We look forward to applying our Ganymede model in support of the recently launched
 1316 JUICE spacecraft, set to enter orbit around the moon in 2034.

1317 **Open Research Section**

1318 The data supporting this work can be obtained from Stahl et al. (2023).

1319 **Acknowledgments**

1320 The authors are grateful to the NASA Solar System Workings 2018 Program (Grant no.
1321 # 80NSSC20K0463) for financial support. We would also like to thank Tyler Tippens
1322 and C. Michael Haynes (both at the Georgia Institute of Technology) for helpful input
1323 on various aspects of this project.

1324 Appendix A Model Validation: Comparison to Galileo Magnetome- 1325 ter Data

1326 To validate the AIKEF hybrid code (introduced in Section 2.1) for modeling Ganymede's
 1327 near-space environment, we apply the model to study magnetometer observations from
 1328 all six Galileo flybys of the moon (see Figure 1). We compare the magnetic field com-
 1329 ponents produced by the model to magnetometer data along each flyby trajectory. The
 1330 model setups for the six Galileo flybys include Ganymede's permanent and induced mag-
 1331 netic dipole moments (see Table A1). However, for this series of simulations, we proceed
 1332 analogous to the hybrid modeling studies of Fatemi et al. (2016, 2022) and Poppe et al.
 1333 (2018) and do not include the moon's atmosphere or ionosphere.

1334 In each model setup, we assume a uniform background magnetic field \mathbf{B}_0 with val-
 1335 ues adopted from Kivelson et al. (2002), see Table A1. For Ganymede's permanent mag-
 1336 netic dipole moment, we adopt the value determined by Kivelson et al. (2002) and de-
 1337 scribed in Section 2.2 (see Table A1). The moon's inductive response is calculated in the
 1338 same way as described in Section 2.2 (see equation (2)). With the exception of the Jo-
 1339 vian plasma density, which varies as a function of Ganymede's distance to the center of
 1340 Jupiter's magnetospheric plasma sheet, we adopt the same upstream parameters as de-
 1341 scribed in Section 2.2. We use a number density of $n_0 = 4 \text{ cm}^{-3}$ when Ganymede is
 1342 located far from the center of the Jovian plasma sheet (G1, G2, G7, G28, and G29), and
 1343 a value of $n_0 = 8 \text{ cm}^{-3}$ when the moon is located close to the center of the sheet (G8).
 1344 These number densities are consistent with the range of 1 to 10 cm^{-3} provided in Jia
 1345 and Kivelson (2021) and similar to the input parameters chosen in the model of Fatemi
 1346 et al. (2022).

1347 In Figure A1, we present the magnetic field components produced by the AIKEF
 1348 model along the six Galileo trajectories and compare them to magnetometer observa-
 1349 tions. As can be seen, the model achieves very good quantitative agreement with both
 1350 the magnitudes and locations of the observed magnetic field perturbations for all three
 1351 components. This further emphasizes that AIKEF is highly suitable to analyze Ganymede's
 1352 magnetospheric interaction during the PJ34 Juno flyby. We refrain from providing a de-
 1353tailed discussion of the model-data comparisons shown in Figure A1. Similar compar-
 1354 isons for the Galileo flybys have already been performed and analyzed in detail by nu-
 1355 merous preceding studies (e.g., Jia et al., 2008, 2009; Duling et al., 2014; Fatemi et al.,

1356 2016, 2022). Therefore, another extensive discussion would not produce any novel phys-
1357 ical insights.

Table A1. Simulation parameters of the AIKEF model for the six Galileo flybys of Ganymede

Parameter	Symbol [units]	G1	G2	G7	G8	G28	G29
Background magnetic field ^a	\mathbf{B}_0 [nT]	(6, -79, -79)	(17, -73, -85)	(-3, 84, -75)	(-11, 11, -77)	(-7, 78, -76)	(-9, -83, -79)
Background field magnitude ^a	B_0 [nT]	111.9	113.3	113.3	78.6	109.1	114.9
Ganymede's Magnetic moment (permanent) ^a	\mathbf{M}_{dip} [$\times 10^{27}$ J/nT]	(-4.1, 9.0, -131.0)	(-4.1, 9.0, -131.0)	(-4.1, 9.0, -131.0)	(-4.1, 9.0, -131.0)	(-4.1, 9.0, -131.0)	(-4.1, 9.0, -131.0)
Ganymede's Magnetic moment (induced) ^a	\mathbf{M}_{ind} [$\times 10^{27}$ J/nT]	(-0.5, 6.1, 0.0)	(-1.3, 5.6, 0.0)	(0.2, -6.4, 0.0)	(0.7, 0.5, 0.0)	(0.5, -6.0, 0.0)	(0.7, 6.4, 0.0)
Upstream plasma number density ^b	n_0 [cm ⁻³]	4	4	4	8	4	4
Upstream plasma mean ion mass ^b	m_0 [amu]	14	14	14	14	14	14
Upstream plasma bulk velocity ^b	\mathbf{u}_0 [km/s]	(140, 0, 0)	(140, 0, 0)	(130, 0, 0)	(140, 0, 0)	(140, 0, 0)	(140, 0, 0)
Upstream plasma ion temperature ^b	$k_B T_0$ [eV]	100	100	100	100	100	100
Upstream plasma electron temperature ^b	$k_B T_0$ [eV]	100	100	100	100	100	100
Convective electric field ^c ($\mathbf{E}_0 = -\mathbf{u}_0 \times \mathbf{B}_0$)	\mathbf{E}_0 [mV/m]	(0,-11.1,11.1)	(0,-11.9,10.2)	(0,-9.9,-10.9)	(0,-10.8,-1.5)	(0,-10.6,-10.9)	(0,-11.1,11.6)
Alfvén velocity ($V_{A,0} = \frac{B_0}{\sqrt{\mu_0 m_0 n_0}})^c$	$V_{A,0}$ [km/s]	326	330	330	162	318	335
Alfvén Mach number ($M_{A,0} = \frac{u_0}{V_{A,0}})^c$	$M_{A,0}$	0.43	0.42	0.39	0.87	0.44	0.42

^a Kivelson et al. (2002)^b Kivelson et al. (2004)^c (calculated)

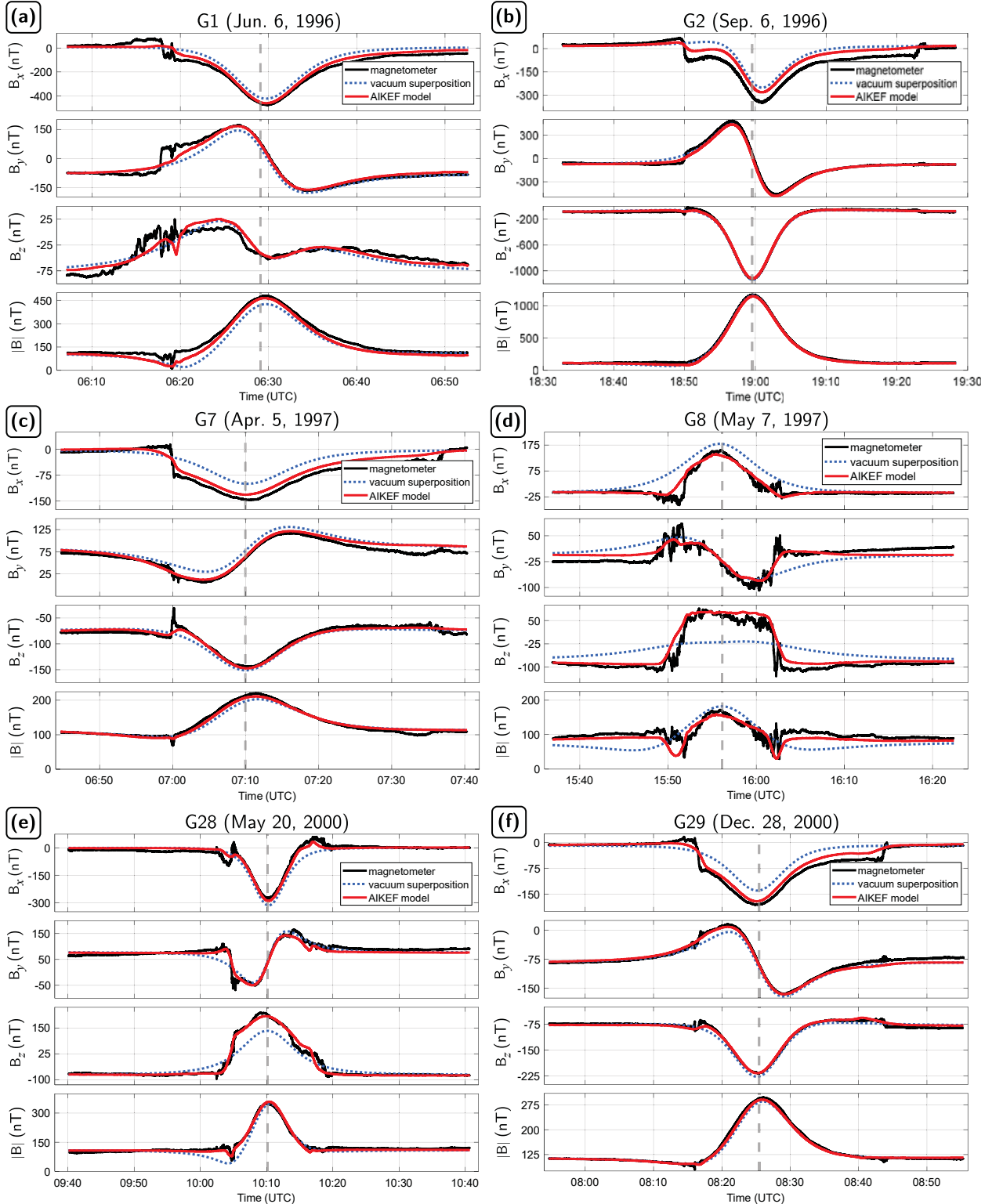


Figure A1. Comparisons of modeled magnetic field components (presented in GPhiO coordinates) from AIKEF (red lines) to Galileo magnetometer observations (black lines) for the six flybys of Ganymede. The flybys are labeled as follows: (a) for G1, (b) for G2, (c) for G7, (d) for G8, (e) for G28, and (f) for G29. In addition to the AIKEF output, we show the magnetic field components obtained by mere superposition of Ganymede's internal field and the magnetospheric background field (called "vacuum superposition" by Kivelson et al. (2002); blue dotted lines). Galileo's closest approach to Ganymede is denoted by a vertical gray dashed line for each flyby. Parameters used for the AIKEF model setup of each flyby can be found in Table A1. Each run includes Ganymede's permanent and induced magnetic dipoles. However, analogous to the approach of Fatemi et al. (2016, 2022) and Poppe et al. (2018), these model runs do not take into account an atmosphere or ionosphere.

1358 **References**

- 1359 Addison, P., Liuzzo, L., Arnold, H., & Simon, S. (2021). Influence of Europa's Time-
 1360 Varying Electromagnetic Environment on Magnetospheric Ion Precipitation
 1361 and Surface Weathering. *Journal of Geophysical Research: Space Physics*,
 1362 *126*(5), e2020JA029087. doi: <https://doi.org/10.1029/2020JA029087>
- 1363 Addison, P., Liuzzo, L., & Simon, S. (2022). Effect of the Magnetospheric Plasma
 1364 Interaction and Solar Illumination on Ion Sputtering of Europa's Surface Ice.
 1365 *Journal of Geophysical Research: Space Physics*, *127*(2), e2021JA030136. doi:
 1366 <https://doi.org/10.1029/2021JA030136>
- 1367 Addison, P., Liuzzo, L., & Simon, S. (2023). Surface-Plasma Interactions at
 1368 Europa in Draped Magnetospheric Fields: The Contribution of Energetic
 1369 Electrons to Energy Deposition and Sputtering. *Journal of Geophysical Re-*
 1370 *search: Space Physics*, *128*(8), e2023JA031734. Retrieved from <https://agupubs.onlinelibrary.wiley.com/doi/abs/10.1029/2023JA031734> doi:
 1371 <https://doi.org/10.1029/2023JA031734>
- 1372 Alday, J., Roth, L., Ivchenko, N., Rutherford, K. D., Becker, T. M., Molyneux, P.,
 1373 & Saur, J. (2017). New constraints on Ganymede's hydrogen corona: Anal-
 1374 ysis of Lyman-alpha emissions observed by HST/STIS between 1998 and
 1375 2014. *Planetary and Space Science*, *148*, 35-44. doi: <https://doi.org/10.1016/j.pss.2017.10.006>
- 1376 Allegrini, F., Bagenal, F., Ebert, R., Louarn, P., Mccomas, D., Szalay, J., ... Waite,
 1377 J. (2022, 07). Plasma observations during the June 7, 2021 Ganymede flyby
 1378 from the Jovian Auroral Distributions Experiment (JADE) on Juno. *Geophys-
 1379 ical Research Letters*. doi: [10.1029/2022GL098682](https://doi.org/10.1029/2022GL098682)
- 1380 Anderson, J. D., Lau, E. L., Sjogren, W. L., Schubert, G., & Moore, W. B. (1996,
 1381 12). Gravitational constraints on the internal structure of Ganymede. *Nature*,
 1382 *384*(6609), 541–543. doi: [10.1038/384541a0](https://doi.org/10.1038/384541a0)
- 1383 Arnold, H., Liuzzo, L., & Simon, S. (2019). Magnetic Signatures of a Plume at Eu-
 1384 ropa During the Galileo E26 Flyby. *Geophysical Research Letters*, *46*(3), 1149–
 1385 1157. doi: [10.1029/2018GL081544](https://doi.org/10.1029/2018GL081544)
- 1386 Arnold, H., Liuzzo, L., & Simon, S. (2020, 1). Plasma Interaction Signatures of
 1387 Plumes at Europa. *Journal of Geophysical Research: Space Physics*, *125*(1).
 1388 doi: [10.1029/2019JA027346](https://doi.org/10.1029/2019JA027346)

- 1391 Arnold, H., Simon, S., & Liuzzo, L. (2020). Applying Ion Energy Spectrograms to
1392 Search for Plumes at Europa. *Journal of Geophysical Research: Space Physics*,
1393 125(9), e2020JA028376. doi: <https://doi.org/10.1029/2020JA028376>
- 1394 Bagena, F., & Delamere, P. A. (2011). Flow of mass and energy in the magne-
1395 tospheres of Jupiter and Saturn. *Journal of Geophysical Research (Space*
1396 *Physics)*, 116(A5), A05209. doi: 10.1029/2010JA016294
- 1397 Bagena, F., Wilson, R. J., Siler, S., Paterson, W. R., & Kurth, W. S. (2016). Sur-
1398 vey of Galileo plasma observations in Jupiter's plasma sheet. *Journal of Geo-*
1399 *physical Research (Planets)*, 121(5), 871–894. doi: 10.1002/2016JE005009
- 1400 Bonfond, B., Hess, S., Bagena, F., Gérard, J.-C., Grodent, D., Radioti, A., ...
1401 Clarke, J. T. (2013). The multiple spots of the Ganymede auroral footprint.
1402 *Geophysical Research Letters*, 40(19), 4977-4981. doi: <https://doi.org/10.1002/grl.50989>
- 1403 Bonfond, B., Saur, J., Grodent, D., Badman, S. V., Bisikalo, D., Shematovich, V.,
1404 ... Radioti, A. (2017). The tails of the satellite auroral footprints at Jupiter.
1405 *Journal of Geophysical Research: Space Physics*, 122(8), 7985-7996. doi:
1406 <https://doi.org/10.1002/2017JA024370>
- 1407 Breer, B. R., Liuzzo, L., Arnold, H., Andersson, P. N., & Simon, S. (2019, 9). Ener-
1408 getic ion dynamics in the perturbed electromagnetic fields near Europa. *Jour-*
1409 *nal of Geophysical Research: Space Physics*, 124(9), 7592–7613. doi: 10.1029/
1410 2019JA027147
- 1411 Buccino, D. R., Parisi, M., Gramigna, E., Gomez-Casajus, L., Tortora, P., Zan-
1412 noni, M., ... Bolton, S. (2022). Ganymede's Ionosphere Observed by a
1413 Dual-Frequency Radio Occultation With Juno. *Geophysical Research Letters*,
1414 49(23), e2022GL098420. doi: <https://doi.org/10.1029/2022GL098420>
- 1415 Carberry Mogan, S. R., Johnson, R. E., Vorburger, A., & Roth, L. (2023). Elec-
1416 tron impact ionization in the icy Galilean satellites' atmospheres. *Eur. Phys.*
1417 *J. D*, 77(2), 26. Retrieved from <https://doi.org/10.1140/epjd/s10053-023-00606-8>
1418 doi: 10.1140/epjd/s10053-023-00606-8
- 1419 Carnielli, G., Galand, M., Leblanc, F., Leclercq, L., Modolo, R., Beth, A., ... Jia,
1420 X. (2019). First 3D test particle model of Ganymede's ionosphere. *Icarus*,
1421 330(October 2017), 42–59. doi: 10.1016/j.icarus.2019.04.016
- 1422 Carnielli, G., Galand, M., Leblanc, F., Modolo, R., Beth, A., & Jia, X. (2020, 6).
- 1423

- 1424 Constraining Ganymede's neutral and plasma environments through simula-
1425 tions of its ionosphere and Galileo observations. *Icarus*, 343, 113691. doi:
1426 10.1016/j.icarus.2020.113691

1427 Cervantes, S., & Saur, J. (2022). Constraining Europa's Subsolar Atmosphere With
1428 a Joint Analysis of HST Spectral Images and Galileo Magnetic Field Data.
1429 *Journal of Geophysical Research: Space Physics*, 127(9), e2022JA030472. doi:
1430 <https://doi.org/10.1029/2022JA030472>

1431 Clark, G., Kollmann, P., Mauk, B. H., Paranicas, C., Haggerty, D., Rymer, A.,
1432 ... Turner, D. L. (2022). Energetic Charged Particle Observations Dur-
1433 ing Juno's Close Flyby of Ganymede. *Geophysical Research Letters*, 49(23),
1434 e2022GL098572. Retrieved from <https://agupubs.onlinelibrary.wiley.com/doi/abs/10.1029/2022GL098572> (e2022GL098572 2022GL098572) doi:
1435 <https://doi.org/10.1029/2022GL098572>

1436 Coates, A. J., Wellbrock, A., Lewis, G. R., Arridge, C. S., Crary, F. J., Young,
1437 D. T., ... Jones, G. H. (2012). Cassini in Titan's tail: CAPS observations
1438 of plasma escape. *Journal of Geophysical Research (Space Physics)*, 117(A5),
1439 A05324. doi: 10.1029/2012JA017595

1440 Connerney, J., Benn, M., Bjarno, J., Denver, T., Espley, J., Jorgensen, J., ... Smith,
1441 E. (2017, 11). The Juno Magnetic Field Investigation. *Space Science Reviews*,
1442 213(1-4), 39-138. doi: 10.1007/s11214-017-0334-z

1443 Connerney, J. E. P., Adriani, A., Allegrini, F., Bagenal, F., Bolton, S. J., Bonfond,
1444 B., ... Waite, J. (2017). Jupiter's magnetosphere and aurorae observed by the
1445 Juno spacecraft during its first polar orbits. *Science*, 356(6340), 826-832. doi:
1446 10.1126/science.aam5928

1447 Cooper, J. F., Johnson, R. E., Mauk, B. H., Garrett, H. B., & Gehrels, N. (2001, 1).
1448 Energetic Ion and Electron Irradiation of the Icy Galilean Satellites. *Icarus*,
1449 149(1), 133–159. doi: 10.1006/icar.2000.6498

1450 Dorelli, J. C., Glocer, A., Collinson, G., & Tóth, G. (2015). The role of the Hall
1451 effect in the global structure and dynamics of planetary magnetospheres:
1452 Ganymede as a case study. *Journal of Geophysical Research A: Space Physics*,
1453 120(7), 5377–5392. doi: 10.1002/2014JA020951

1454 Duling, S., Saur, J., Clark, G., Allegrini, F., Greathouse, T., Gladstone, R., ...
1455 Sulaiman, A. H. (2022). Ganymede MHD Model: Magnetospheric Con-

- 1457 text for Juno's PJ34 Flyby. *Geophysical Research Letters*, 49(24). doi:
1458 <https://doi.org/10.1029/2022GL101688>
- 1459 Duling, S., Saur, J., & Wicht, J. (2014). Consistent boundary conditions at noncon-
1460 ducting surfaces of planetary bodies: Applications in a new Ganymede MHD
1461 model. *Journal of Geophysical Research: Space Physics*, 119(6), 4412–4440.
1462 doi: 10.1002/2013JA019554
- 1463 Eviatar, A., Strobel, D. F., Wolven, B. C., Feldman, P. D., McGrath, M. A., &
1464 Williams, D. J. (2001, 7). Excitation of the Ganymede ultraviolet aurora. *The
1465 Astrophysical Journal*, 555(2), 1013. doi: 10.1086/321510
- 1466 Eviatar, A., Vasyliunas, V. M., & Gurnett, D. A. (2001, 3). The ionosphere
1467 of Ganymede. *Planetary and Space Science*, 49(3-4), 327–336. doi:
1468 [https://doi.org/10.1016/S0032-0633\(00\)00154-9](https://doi.org/10.1016/S0032-0633(00)00154-9)
- 1469 Eviatar, A., Williams, D. J., Paranicas, C., McEntire, R. W., Mauk, B. H., & Kivel-
1470 son, M. G. (2000). Trapped Energetic Electrons in the Magnetosphere of
1471 Ganymede. *Journal of Geophysical Research: Space Physics*, 105(A3), 5547–
1472 5553. doi: 10.1029/1999ja900450
- 1473 Fatemi, S., Poppe, A. R., Khurana, K. K., Holmström, M., & Delory, G. T. (2016).
1474 On the formation of Ganymede's surface brightness asymmetries: Kinetic sim-
1475 ulations of Ganymede's magnetosphere. *Geophysical Research Letters*, 43(10),
1476 4745–4754. doi: 10.1002/2016GL068363
- 1477 Fatemi, S., Poppe, A. R., Vorburger, A., Lindkvist, J., & Hamrin, M. (2022).
1478 Ion Dynamics at the Magnetopause of Ganymede. *Journal of Geophys-
1479 ical Research: Space Physics*, 127(1). Retrieved from <https://agupubs.onlinelibrary.wiley.com/doi/abs/10.1029/2021JA029863> doi:
1480 <https://doi.org/10.1029/2021JA029863>
- 1482 Feldman, P. D., McGrath, M. A., Strobel, D. F., Moos, H. W., Rutherford, K. D.,
1483 & Wolven, B. C. (2000, 6). HST/STIS ultraviolet imaging of polar au-
1484 rora on Ganymede. *The Astrophysical Journal*, 535(2), 1085–1090. doi:
1485 10.1086/308889
- 1486 Feyerabend, M., Simon, S., Motschmann, U., & Liuzzo, L. (2015). Filamented ion
1487 tail structures at Titan: A hybrid simulation study. *Planetary and Space Sci-
1488 ence*, 117, 362–376. doi: 10.1016/j.pss.2015.07.008
- 1489 Frank, L. A., Paterson, W. R., Ackerson, K. L., & Bolton, S. J. (1997, 9). Low-

- 1490 energy electron measurements at Ganymede with the Galileo spacecraft:
1491 Probes of the magnetic topology. *Geophysical Research Letters*, 24(17), 2159–
1492 2162. doi: 10.1029/97GL01632
- 1493 Greathouse, T. K., Gladstone, G. R., Molyneux, P. M., Versteeg, M. H., Hue, V.,
1494 Kammer, J. A., ... Duling, S. (2022). UVS Observations of Ganymede's Au-
1495 rora During Juno Orbits 34 and 35. *Geophysical Research Letters*, 49(23). doi:
1496 <https://doi.org/10.1029/2022GL099794>
- 1497 Grodent, D., Bonfond, B., Radioti, A., Gérard, J.-C., Jia, X., Nichols, J. D., &
1498 Clarke, J. T. (2009). Auroral footprint of Ganymede. *Journal of Geo-
1499 physical Research: Space Physics*, 114(A7). doi: <https://doi.org/10.1029/2009JA014289>
- 1500 Gurnett, D. A., Kurth, W. S., Roux, A., Bolton, S. J., & Kennel, C. F. (1996, 12).
1501 Evidence for a magnetosphere at Ganymede from plasma-wave observations by
1502 the Galileo spacecraft. *Nature*, 384(6609), 535–537. doi: 10.1038/384535a0
- 1503 Hall, D. T., Feldman, P. D., McGrath, M. A. M. A., & Strobel, D. F. (1998). The
1504 Far-Ultraviolet Oxygen Airglow of Europa and Ganymede. *The Astrophysical
1505 Journal*, 499(1), 475–481. doi: 10.1086/305604
- 1506 Hansen, C. J., Bolton, S., Sulaiman, A. H., Duling, S., Bagenal, F., Brennan, M.,
1507 ... Withers, P. (2022). Juno's Close Encounter With Ganymede—An
1508 Overview. *Geophysical Research Letters*, 49(23). doi: <https://doi.org/10.1029/2022GL099285>
- 1509 Hue, V., Szalay, J. R., Greathouse, T. K., Bonfond, B., Kotsiaros, S., Louis, C. K.,
1510 ... Mauk, B. H. (2022). A Comprehensive Set of Juno In Situ and Re-
1511 mote Sensing Observations of the Ganymede Auroral Footprint. *Geophys-
1512 ical Research Letters*, 49(7), e2021GL096994. doi: <https://doi.org/10.1029/2021GL096994>
- 1513 Ip, W.-H., & Kopp, A. (2002). Resistive MHD simulations of Ganymede's magne-
1514 tosphere 2. Birkeland currents and particle energetics. *Journal of Geophysical
1515 Research: Space Physics*, 107(A12), SMP 42-1-SMP 42-7. doi: <https://doi.org/10.1029/2001JA005072>
- 1516 Jia, X., & Kivelson, M. G. (2021). The Magnetosphere of Ganymede. In *Mag-
1517 netospheres in the solar system* (p. 557-573). American Geophysical Union
1518 (AGU). Retrieved from <https://agupubs.onlinelibrary.wiley.com/>
- 1519
- 1520
- 1521
- 1522

- 1523 doi/abs/10.1002/9781119815624.ch35 doi: <https://doi.org/10.1002/9781119815624.ch35>
- 1524
- 1525 Jia, X., Walker, R. J., Kivelson, M. G., Khurana, K. K., & Linker, J. A. (2008, 6).
1526 Three-dimensional MHD simulations of Ganymede's magnetosphere. *Journal of
1527 Geophysical Research: Space Physics*, 113(6). doi: 10.1029/2007JA012748
- 1528 Jia, X., Walker, R. J., Kivelson, M. G., Khurana, K. K., & Linker, J. A. (2009).
1529 Properties of Ganymede's magnetosphere inferred from improved three-
1530 dimensional MHD simulations. *Journal of Geophysical Research: Space
1531 Physics*, 114(9). doi: 10.1029/2009JA014375
- 1532 Jia, X., Walker, R. J., Kivelson, M. G., Khurana, K. K., & Linker, J. A. (2010). Dy-
1533 namics of Ganymede's magnetopause: Intermittent reconnection under steady
1534 external conditions. *Journal of Geophysical Research: Space Physics*, 115(12).
1535 doi: 10.1029/2010JA015771
- 1536 Joy, S. P., Kivelson, M. G., Walker, R. J., Khurana, K. K., Russell, C. T., & Ogino,
1537 T. (2002, 10). Probabilistic models of the Jovian magnetopause and bow shock
1538 locations. *Journal of Geophysical Research (Space Physics)*, 107(A10), 1309.
1539 doi: 10.1029/2001JA009146
- 1540 Kaweeyanun, N., Masters, A., & Jia, X. (2020). Favorable Conditions for Magnetic
1541 Reconnection at Ganymede's Upstream Magnetopause. *Geophysical Research
1542 Letters*, 47(6), 0–3. doi: 10.1029/2019GL086228
- 1543 Kaweeyanun, N., Masters, A., & Jia, X. (2021). Analytical Assessment of Kelvin-
1544 Helmholtz Instability Growth at Ganymede's Upstream Magnetopause. *Jour-
1545 nal of Geophysical Research: Space Physics*, 126(8), e2021JA029338. doi:
1546 <https://doi.org/10.1029/2021JA029338>
- 1547 Khurana, K. K., Pappalardo, R., Murphy, N., & Denk, T. (2007, 11). The origin of
1548 Ganymede's polar caps. *Icarus*, 191(1), 193–202. doi: 10.1016/j.icarus.2007.04
1549 .022
- 1550 Kim, T. K., Ebert, R. W., Valek, P. W., Allegrini, F., McComas, D. J., Bagenal, F.,
1551 ... Bolton, S. J. (2020). Survey of Ion Properties in Jupiter's Plasma Sheet:
1552 Juno JADE-I Observations. *Journal of Geophysical Research: Space Physics*,
1553 125(4), e2019JA027696. doi: <https://doi.org/10.1029/2019JA027696>
- 1554 Kivelson, M., Bagenal, F., Kurth, W., Neubauer, F., Paranicas, C., & Saur, J.
1555 (2004). Magnetospheric interactions with satellites. *Jupiter: The planet*,

- 1556 *satellites and magnetosphere*, *m*, 513–536.
- 1557 Kivelson, M., Khurana, K. K., Russell, C. T., Walker, R. J., Warnecke, J., Coroniti,
 1558 F. V., ... Schubert, G. (1996). Discovery of Ganymede's magnetic field by the
 1559 Galileo spacecraft. *Nature*, *384*(6609), 537–541. doi: 10.1038/384537a0
- 1560 Kivelson, M., Khurana, K. K., & Volwerk, M. (2002, 6). The permanent and induc-
 1561 tive magnetic moments of Ganymede. *Icarus*, *157*(2), 507–522. doi: 10.1006/
 1562 icar.2002.6834
- 1563 Kivelson, M., Warnecke, J., Bennett, L., Joy, S., Khurana, K. K., Linker, J. A., ...
 1564 Polanskey, C. (1998). Ganymede's magnetosphere: Magnetometer overview.
 1565 *Journal of Geophysical Research: Planets*, *103*(E9), 19963–19972. Retrieved
 1566 from <https://agupubs.onlinelibrary.wiley.com/doi/abs/10.1029/98JE00227> doi: <https://doi.org/10.1029/98JE00227>
- 1567 Kliore, A. J. (1998). Satellite Atmospheres and Magnetospheres. In J. Andersen
 1568 (Ed.), *Highlights of astronomy: As presented at the xxiiird general assembly*
 1569 of the iau, 1997 (pp. 1065–1069). Dordrecht: Springer Netherlands. doi:
 1570 10.1007/978-94-011-4778-1_138
- 1571 Kriegel, H., Simon, S., Meier, P., Motschmann, U., Saur, J., Wennmacher, A., ...
 1572 Dougherty, M. K. (2014). Ion densities and magnetic signatures of dust pick-
 1573 up at Enceladus. *Journal of Geophysical Research (Space Physics)*, *119*(4),
 1574 2740–2774. doi: 10.1002/2013JA019440
- 1575 Kriegel, H., Simon, S., Motschmann, U., Saur, J., Neubauer, F. M., Persoon, A. M.,
 1576 ... Gurnett, D. a. (2011). Influence of negatively charged plume grains on
 1577 the structure of Enceladus' Alfvén wings: Hybrid simulations versus Cassini
 1578 Magnetometer data. *Journal of Geophysical Research: Space Physics*, *116*(10),
 1579 1–19. doi: 10.1029/2011JA016842
- 1580 Krupp, N., Vasyliūnas, V., Woch, J., Lagg, A., Khurana, K., Kivelson, M., ... Pa-
 1581 terson, W. (2004, 01). The Dynamics of the Jovian magnetosphere. *Jupiter:*
 1582 *The Planet, Satellites and Magnetosphere*, 617–638 (2004).
- 1583 Kurth, W., Hospodarsky, G., Kirchner, D., Mokrzycki, B., Averkamp, T., Robison,
 1584 W., ... Zarka, P. (2017, 11). The Juno Waves Investigation. *Space Science*
 1585 *Reviews*, *213*. doi: 10.1007/s11214-017-0396-y
- 1586 Kurth, W., Sulaiman, A., Hospodarsky, G., Mauk, J., & Clark, G. (2022). Juno
 1587 Plasma Wave Observations at Ganymede. *Geophysical Research Letters*,

- 1589 *n/a(n/a)*. doi: <https://doi.org/10.1029/2022GL098591>
- 1590 Leblanc, F., Oza, A. V., Leclercq, L., Schmidt, C., Cassidy, T., Modolo, R., ...
- 1591 Johnson, R. E. (2017, 9). On the orbital variability of Ganymede's atmo-
1592 sphere. *Icarus*, 293, 185–198. doi: 10.1016/j.icarus.2017.04.025
- 1593 Leblanc, F., Roth, L., Chaufray, J., Modolo, R., Galand, M., Ivchenko, N., ...
- 1594 Werner, A. (2023). Ganymede's atmosphere as constrained by HST/STIS ob-
1595 servations. *Icarus*, 115557. doi: <https://doi.org/10.1016/j.icarus.2023.115557>
- 1596 Liuzzo, L., Feyerabend, M., Simon, S., & Motschmann, U. (2015). The impact
1597 of Callisto's atmosphere on its plasma interaction with the Jovian magneto-
1598 sphere. *Journal of Geophysical Research A: Space Physics*, 120(11), 9401–
1599 9427. doi: 10.1002/2015JA021792
- 1600 Liuzzo, L., Poppe, A. R., Addison, P., Simon, S., Nénon, Q., & Paranicas, C. (2022).
1601 Energetic Magnetospheric Particle Fluxes Onto Callisto's Atmosphere. *Jour-*
1602 *nal of Geophysical Research: Space Physics*, 127(11), e2022JA030915. doi:
1603 <https://doi.org/10.1029/2022JA030915>
- 1604 Liuzzo, L., Poppe, A. R., Paranicas, C., Nénon, Q., Fatemi, S., & Simon, S. (2020).
1605 Variability in the Energetic Electron Bombardment of Ganymede. *Journal of*
1606 *Geophysical Research: Space Physics*, 125(9), e2020JA028347. doi: <https://doi.org/10.1029/2020JA028347>
- 1607 Liuzzo, L., Simon, S., & Feyerabend, M. (2018). Observability of Callisto's Inductive
1608 Signature During the JUpiter ICy Moons Explorer Mission. *Journal of Geo-*
1609 *physical Research: Space Physics*, 123(11), 9045–9054. doi: <https://doi.org/10.1029/2018JA025951>
- 1610 Liuzzo, L., Simon, S., Feyerabend, M., & Motschmann, U. (2016). Disentangling
1611 plasma interaction and induction signatures at Callisto: The Galileo C10 flyby.
1612 *Journal of Geophysical Research: Space Physics*, 121(9), 8677–8694. doi:
1613 10.1002/2016JA023236
- 1614 Liuzzo, L., Simon, S., Feyerabend, M., & Motschmann, U. (2017). Magnetic signa-
1615 tures of plasma interaction and induction at Callisto: The Galileo C21, C22,
1616 C23, and C30 flybys. *Journal of Geophysical Research: Space Physics*, 122(7),
1617 7364–7386. doi: 10.1002/2017JA024303
- 1618 Liuzzo, L., Simon, S., & Regoli, L. (2019a). Energetic electron dynamics near Cal-
1619 listo. *Planetary and Space Science*, 179, 104726. doi: <https://doi.org/10.1016/>

- 1622 j.pss.2019.104726
- 1623 Liuzzo, L., Simon, S., & Regoli, L. (2019b, 2). Energetic ion dynamics near Callisto.
 1624 *Planetary and Space Science*, 166, 23–53. doi: 10.1016/j.pss.2018.07.014
- 1625 Marconi, M. L. (2007, 9). A kinetic model of Ganymede’s atmosphere. *Icarus*,
 1626 190(1), 155–174. doi: 10.1016/j.icarus.2007.02.016
- 1627 Masters, A. (2017). Model-Based Assessments of Magnetic Reconnection
 1628 and Kelvin-Helmholtz Instability at Jupiter’s Magnetopause. *Journal*
 1629 *of Geophysical Research: Space Physics*, 122(11), 11,154-11,174. doi:
 1630 <https://doi.org/10.1002/2017JA024736>
- 1631 Mauk, B. H., Mitchell, D. G., McEntire, R. W., Paranicas, C. P., Roelof, E. C.,
 1632 Williams, D. J., ... Lagg, A. (2004). Energetic ion characteristics and neutral
 1633 gas interactions in Jupiter’s magnetosphere. *Journal of Geophysical Research:*
 1634 *Space Physics*, 109(A9). doi: 10.1029/2003JA010270
- 1635 McComas, D. J., Alexander, N., Allegrini, F., Bagenal, F., Beebe, C. R., Clark, G.,
 1636 ... White, D. (2017). The Jovian Auroral Distributions Experiment (JADE)
 1637 on the Juno Mission to Jupiter. *Space Science Reviews*, 213, 547-643.
- 1638 McGrath, M. A., Jia, X., Retherford, K., Feldman, P. D., Strobel, D. F., & Saur, J.
 1639 (2013). Aurora on Ganymede. *Journal of Geophysical Research: Space Physics*,
 1640 118(5), 2043–2054. doi: 10.1002/jgra.50122
- 1641 Molyneux, P. M., Nichols, J. D., Bannister, N. P., Bunce, E. J., Clarke, J. T.,
 1642 Cowley, S. W. H., ... Paty, C. (2018). Hubble Space Telescope Ob-
 1643 servations of Variations in Ganymede’s Oxygen Atmosphere and Aurora.
 1644 *Journal of Geophysical Research: Space Physics*, 123(5), 3777-3793. doi:
 1645 <https://doi.org/10.1029/2018JA025243>
- 1646 Müller, J., Simon, S., Motschmann, U., Schüle, J., Glassmeier, K. H., & Pringle,
 1647 G. J. (2011). A.I.K.E.F.: Adaptive hybrid model for space plasma sim-
 1648 ulations. *Computer Physics Communications*, 182(4), 946–966. Re-
 1649 trieved from <http://dx.doi.org/10.1016/j.cpc.2010.12.033> doi:
 1650 10.1016/j.cpc.2010.12.033
- 1651 Müller, J., Simon, S., Wang, Y.-C., Motschmann, U., Heyner, D., Schüle, J., ...
 1652 Pringle, G. J. (2012). Origin of Mercury’s double magnetopause: 3D
 1653 hybrid simulation study with A.I.K.E.F. *Icarus*, 218(1), 666-687. doi:
 1654 <https://doi.org/10.1016/j.icarus.2011.12.028>

- 1655 Neubauer, F. M. (1980). Nonlinear standing Alfvén wave current system at
 1656 Io: Theory. *Journal of Geophysical Research*, *85*(9), 1171. doi: 10.1029/
 1657 JA085iA03p01171
- 1658 Neubauer, F. M. (1998). The sub-Alfvénic interaction of the Galilean satellites with
 1659 the Jovian magnetosphere. *Journal of Geophysical Research (Space Physics)*,
 1660 *103*, 19843–19866. doi: 10.1029/97JE03370
- 1661 Neubauer, F. M. (1999). Alfvén wings and electromagnetic induction in the interi-
 1662 ors: Europa and Callisto. *Journal of Geophysical Research*, *104*, 28671. doi: 10
 1663 .1029/1999JA900217
- 1664 Paty, C., Paterson, W., & Winglee, R. (2008, 6). Ion energization in Ganymede's
 1665 magnetosphere: Using multifluid simulations to interpret ion energy spec-
 1666 trograms. *Journal of Geophysical Research: Space Physics*, *113*(6). doi:
 1667 10.1029/2007JA012848
- 1668 Paty, C., & Winglee, R. (2004, 1). Multi-fluid simulations of Ganymede's mag-
 1669 netosphere. *Geophysical Research Letters*, *31*(24), 1–5. doi: 10.1029/
 1670 2004GL021220
- 1671 Paty, C., & Winglee, R. (2006, 5). The role of ion cyclotron motion at Ganymede:
 1672 Magnetic field morphology and magnetospheric dynamics. *Geophysical Re-
 1673 search Letters*, *33*(10). doi: 10.1029/2005GL025273
- 1674 Payan, A. P., Paty, C. S., & Rutherford, K. D. (2015). Uncovering local magne-
 1675 tospheric processes governing the morphology and variability of Ganymede's
 1676 aurora using three-dimensional multifluid simulations of Ganymede's magneto-
 1677 sphere. *Journal of Geophysical Research: Space Physics*, *120*(1), 401–413. doi:
 1678 10.1002/2014JA020301
- 1679 Plainaki, C., Milillo, A., Massetti, S., Mura, A., Jia, X., Orsini, S., ... Rispoli, R.
 1680 (2015, 1). The H₂O and O₂ exospheres of Ganymede: The result of a complex
 1681 interaction between the jovian magnetospheric ions and the icy moon. *Icarus*,
 1682 *245*, 306–319. doi: 10.1016/j.icarus.2014.09.018
- 1683 Poppe, A. R., Fatemi, S., & Khurana, K. K. (2018, 6). Thermal and energetic ion
 1684 dynamics in Ganymede's magnetosphere. *Journal of Geophysical Research:*
 1685 *Space Physics*, *123*(6), 4614–4637. doi: 10.1029/2018JA025312
- 1686 Romanelli, N., DiBraccio, G. A., Modolo, R., Connerney, J. E. P., Ebert, R. W.,
 1687 Martos, Y. M., ... Bolton, S. J. (2022). Juno Magnetometer Observations

- 1688 at Ganymede: Comparisons With a Global Hybrid Simulation and Indications
1689 of Magnetopause Reconnection. *Geophysical Research Letters*, 49(23). doi:
1690 <https://doi.org/10.1029/2022GL099545>
- 1691 Roth, L. (2021). A Stable H₂O Atmosphere on Europa's Trailing Hemisphere From
1692 HST Images. *Geophysical Research Letters*, 48(20), e2021GL094289. doi:
1693 <https://doi.org/10.1029/2021GL094289>
- 1694 Roth, L., Ivchenko, N., Gladstone, G., Saur, J., Grodent, D., Bonfond, B., ...
1695 Rutherford, K. (2021, 10). A sublimated water atmosphere on Ganymede
1696 detected from Hubble Space Telescope observations. *Nature Astronomy*, 5.
1697 doi: 10.1038/s41550-021-01426-9
- 1698 Roth, L., Marchesini, G., Becker, T. M., Hoeijmakers, H. J., Molyneux, P. M.,
1699 Rutherford, K. D., ... Szalay, J. R. (2023, jan). Probing Ganymede's Atmo-
1700 sphere with HST Ly-alpha Images in Transit of Jupiter. *The Planetary Science
1701 Journal*, 4(1), 12. doi: 10.3847/PSJ/acaf7f
- 1702 Saur, J., Duling, S., Roth, L., Jia, X., Strobel, D. F., Feldman, P. D., ... Hartkorn,
1703 O. (2015, 3). The search for a subsurface ocean in Ganymede with Hub-
1704 ble Space Telescope observations of its auroral ovals. *Journal of Geophysical
1705 Research: Space Physics*, 120(3), 1715–1737. doi: 10.1002/2014JA020778
- 1706 Saur, J., Neubauer, F. M., & Glassmeier, K.-H. H. (2010). Induced magnetic fields
1707 in solar system bodies. *Space Science Reviews*, 152(1-4), 391–421. doi: 10
1708 .1007/s11214-009-9581-y
- 1709 Schubert, G., Zhang, K., Kivelson, M. G., & Anderson, J. D. (1996). The magnetic
1710 field and internal structure of Ganymede. *Nature*, 384(6609), 544–545. doi: 10
1711 .1038/384544a0
- 1712 Shematovich, V. (2016, 07). Neutral atmosphere near the icy surface of
1713 Jupiter's moon Ganymede. *Solar System Research*, 50, 262-280. doi:
1714 10.1134/S0038094616040067
- 1715 Simon, S., Addison, P., & Liuzzo, L. (2022). Formation of a Displaced Plasma Wake
1716 at Neptune's Moon Triton. *Journal of Geophysical Research: Space Physics*,
1717 127(1), e2021JA029958. doi: <https://doi.org/10.1029/2021JA029958>
- 1718 Simon, S., Boesswetter, a., Bagdonat, T., Motschmann, U., & Schuele, J. (2007).
1719 Three-dimensional multispecies hybrid simulation of Titan's highly vari-
1720 able plasma environment. *Annales Geophysicae*, 25(1), 117–144. doi:

- 10.5194/angeo-25-117-2007
- 1721 Stahl, A., Addison, P., Simon, S., & Liuzzo, L. (2023). Data for “A
1722 model of Ganymede’s magnetic and plasma environment during
1723 the Juno PJ34 flyby” by Stahl et al., 2023 [Data set]. *Zenodo*,
1724 <https://doi.org/10.5281/zenodo.8370898>. doi: 10.5281/zenodo.8370898
- 1725 Szego, K., Bebesi, Z., Bertucci, C., Coates, A. J., Crary, F., Erdos, G., ... Young,
1726 D. T. (2007). Charged particle environment of Titan during the T9 flyby.
1727 *Geophys. Res. Lett.*, 34(24), L24S03. doi: 10.1029/2007GL030677
- 1728 Tippens, T., Liuzzo, L., & Simon, S. (2022). Influence of Titan’s Variable Electro-
1729 magnetic Environment on the Global Distribution of Energetic Neutral Atoms.
1730 *Journal of Geophysical Research: Space Physics*, 127(10), e2022JA030722. doi:
1731 <https://doi.org/10.1029/2022JA030722>
- 1732 Tóth, G., Jia, X., Markidis, S., Peng, I. B., Chen, Y., Daldorff, L. K. S., ... Dorelli,
1733 J. C. (2016, 2). Extended magnetohydrodynamics with embedded particle-
1734 in-cell simulation of Ganymede’s magnetosphere. *Journal of Geophysical
1735 Research: Space Physics*, 121(2), 1273–1293. doi: 10.1002/2015JA021997
- 1736 Turc, L., Leclercq, L., Leblanc, F., Modolo, R., & Chaufray, J.-Y. (2014). Modelling
1737 Ganymede’s neutral environment: A 3D test-particle simulation. *Icarus*, 229,
1738 157–169. doi: <https://doi.org/10.1016/j.icarus.2013.11.005>
- 1739 Valek, P. W., Waite, J. H., Allegrini, F., Ebert, R. W., Bagena, F., Bolton,
1740 S. J., ... Wilson, R. J. (2022). In Situ Ion Composition Observations of
1741 Ganymede’s Outflowing Ionosphere. *Geophysical Research Letters*, 49(24). doi:
1742 <https://doi.org/10.1029/2022GL100281>
- 1743 Volwerk, M., Kivelson, M. G., Khurana, K. K., & McPherron, R. L. (1999, 7). Prob-
1744 ing Ganymede’s magnetosphere with field line resonances. *Journal of Geophys-
1745 ical Research: Space Physics*, 104(A7), 14729–14738. Retrieved from <http://doi.wiley.com/10.1029/1999JA900161> doi: 10.1029/1999JA900161
- 1746 Vorburger, A., Fatemi, S., Galli, A., Liuzzo, L., Poppe, A. R., & Wurz, P. (2022).
1747 3D Monte-Carlo simulation of Ganymede’s water exosphere. *Icarus*, 375,
1748 114810. doi: <https://doi.org/10.1016/j.icarus.2021.114810>
- 1749 Wang, L., Germaschewski, K., Hakim, A., Dong, C., Raeder, J., & Bhattacharjee,
1750 A. (2018, 4). Electron Physics in 3-D Two-Fluid 10-Moment Modeling of
1751 Ganymede’s Magnetosphere. *Journal of Geophysical Research: Space Physics*,

- 1754 123(4), 2815–2830. doi: 10.1002/2017JA024761
- 1755 Weber, T., Moore, K., Connerney, J., Espley, J., DiBraccio, G., & Romanelli,
1756 N. (2022). Updated Spherical Harmonic Magnetic Field Moments of
1757 Ganymede From the Juno Flyby. *Geophysical Research Letters*, 49(23). doi:
1758 <https://doi.org/10.1029/2022GL098633>
- 1759 Williams, D. J., Mauk, B., & McEntire, R. W. (1997). Trapped electrons in
1760 Ganymede's magnetic field. *Geophysical Research Letters*, 24(23), 2953–2956.
1761 doi: 10.1029/97GL03003
- 1762 Williams, D. J., Mauk, B. H., McEntire, R. W., Roelof, E. C., Armstrong, T. P.,
1763 Wilken, B., ... others (1997). Energetic particle signatures at Ganymede: Im-
1764 plications for Ganymede's magnetic field. *Geophysical research letters*, 24(17),
1765 2163–2166. doi: 10.1029/97GL01931
- 1766 Zhou, H., Tóth, G., Jia, X., Chen, Y., & Markidis, S. (2019, 5). Embedded Ki-
1767 netic Simulation of Ganymede's Magnetosphere: Improvements and Inferences.
1768 *Journal of Geophysical Research: Space Physics*, 124(7), 5441–5460. doi:
1769 10.1029/2019ja026643